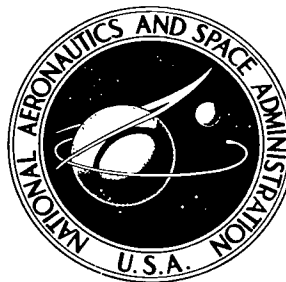


NASA TECHNICAL NOTE



NASA TN D-4693

c.1

NASA TN D-4693



LOAN COPY: RETURN TO
AFWL (WL0L-2)
KIRTLAND AFB, N MEX

**A WIND-TUNNEL INVESTIGATION OF
JET-WAKE EFFECT OF A HIGH-BYPASS ENGINE
ON WING-NACELLE INTERFERENCE DRAG
OF A SUBSONIC TRANSPORT**

by James C. Patterson, Jr.

Langley Research Center

Langley Station, Hampton, Va.



A WIND-TUNNEL INVESTIGATION OF JET-WAKE EFFECT OF
A HIGH-BYPASS ENGINE ON WING-NACELLE INTERFERENCE
DRAG OF A SUBSONIC TRANSPORT

By James C. Patterson, Jr.

Langley Research Center
Langley Station, Hampton, Va.

NATIONAL AERONAUTICS AND SPACE ADMINISTRATION

For sale by the Clearinghouse for Federal Scientific and Technical Information
Springfield, Virginia 22151 - CFSTI price \$3.00

A WIND-TUNNEL INVESTIGATION OF JET-WAKE EFFECT OF
A HIGH-BYPASS ENGINE ON WING-NACELLE INTERFERENCE
DRAG OF A SUBSONIC TRANSPORT

By James C. Patterson, Jr.
Langley Research Center

SUMMARY

An experimental wind-tunnel investigation has been conducted recently by the National Aeronautics and Space Administration to determine the aerodynamic interference associated with underwing fan-jet engine-pylon installations including the effect of a jet wake from a powered high-bypass fan-jet engine. Tests were made on a semispan model of a typical transport airplane configuration. These tests were conducted over a Mach number range of 0.70 to 0.84, at angles of attack from 0° to 4° , and over a Reynolds number range of 6.67×10^6 to 7.38×10^6 based on the mean geometric chord of 58.30 centimeters.

The data indicate that the interference drag for the type of underwing engine-pylon installation investigated may be favorable as a result of a reduction in induced drag associated with an inboard end-plate effect of the nacelle-pylon. The addition of engine power has a strong influence on aerodynamic interference. The longitudinal and vertical position of the engine relative to the wing also has a pronounced effect on interference drag. The greatest favorable interference was obtained during this investigation with the engine in the most forward longitudinal and lowest vertical test position. An increase in Mach number above the design speed has an adverse influence on the aerodynamic interference.

INTRODUCTION

The relatively large size of the high-bypass fan-jet engines to be used on the next generation of subsonic transport aircraft has raised the question as to whether such engines will result in severe adverse wing-nacelle interference. Exploratory tests made with flow-through nacelles, which simulated the engine geometric effect but not the fan-jet wake effects, have indicated no special wing-nacelle interference problems associated with the use of such engines. However, the jet wake may have strong influence on the interference phenomena.

To provide a preliminary indication of the jet-wake effect on wing-nacelle interference for high-bypass engines, an exploratory wind-tunnel investigation of the problem

has been performed in the Langley 8-foot transonic pressure tunnel. In this investigation, the jet wake has been simulated by a model jet engine capable of producing the same relative mass flow and pressure ratios as a representative full-scale high-bypass engine. The investigation was made on a semispan model of a representative transport airplane configuration with the model engine located at various longitudinal and vertical positions relative to the wing at one spanwise wing station. These tests were performed at Mach numbers ranging from 0.70 to 0.84 and over an angle-of-attack range of 0° to 4°.

SYMBOLS

A	cross-sectional area, meters ²
C _D	drag coefficient, Drag/qS
ΔC _D	interference-drag coefficient
C _{F,n}	net-thrust coefficient, F _n /qS
C _L	lift coefficient, Lift/qS
C _p	pressure coefficient, $\frac{p_l - p_\infty}{q}$
ΔC _p	differential pressure coefficient
c	chord at wing-pylon juncture, 60.07 centimeters
\bar{c}	mean geometric chord, 58.30 centimeters
c _f	local skin-friction coefficient
D _R	ram drag, newtons
D _S	scrubbing drag, newtons
F _{g,f}	fan gross thrust, measured at fan exit, newtons
F _{g,p}	primary gross thrust, measured at turbine exit, newtons
F _n	net thrust, newtons

i_w	wing angle of incidence, degrees
$K_{m,i}$	inlet mass-flow correction
M	free-stream Mach number
\dot{m}	mass-flow rate, kilograms/second
p	static pressure, newtons/meter ²
p_t	total pressure, newtons/meter ²
q	free-stream dynamic pressure, newtons/meter ²
R	gas constant ($R_{\text{air}} = 0.287$ joule/ ^o K-mole; $R_{\text{nitrogen}} = 0.298$ joule/ ^o K-mole)
r	radius, centimeters
S	wing reference area, 0.776 meter ²
T	temperature, degrees Kelvin
V	velocity, meters/second
x	longitudinal wing ordinate measured in axial direction (positive downstream), centimeters
y	spanwise station, centimeters
α	angle of attack, degrees
γ	specific-heat ratio ($\gamma_{\text{air}} = 1.4$; $\gamma_{\text{nitrogen}} = 1.41$)
θ	circumferential position, measured clockwise from vertical, degrees
ρ	density, kilograms/meter ³

Subscripts:

av	average
e	exit
i	inlet
l	local
p	primary
s	static
t	total
wet	wetted area
∞	free stream

APPARATUS AND EXPERIMENTAL METHODS

Test Facility

The investigation was conducted in the Langley 8-foot transonic pressure tunnel, which is capable of continuous operation through the subsonic, transonic, and low supersonic speed ranges. The test section of the wind tunnel has a slotted floor and ceiling with solid side walls as shown in figure 1. The slots reduce the wall interference; this reduction allows tests of relatively large models at the subsonic speeds. (See ref. 1.) The model used in the present investigation has a wing semispan equal to 65 percent of the tunnel width and a frontal area equal to 3.4 percent of the tunnel test-section area.

Model Configuration

A drawing of the semispan model used during this investigation is shown in figure 2. A photograph of the model installed in the wind tunnel is shown in figure 3. The choice of a semispan configuration for this investigation has allowed the use of a much larger scale model than normally tested in the Langley 8-foot transonic pressure tunnel at subsonic speeds. Using the semispan model results in a larger, more practical model-engine size and a more satisfactory feed of the engine-drive fluid. Furthermore, since only one-half

the number of model engines are required, the problems associated with engine installation, engine control, and instrumentation are reduced.

Wing.- The wing, shown in figure 2, has a quarter-chord sweep of 35° , a taper ratio of 0.45, and an aspect ratio of 5. This wing, having a semispan of 139.47 centimeters, simulates the inboard portion of a higher aspect-ratio wing which had a semispan of 190.88 centimeters. It is believed that the removal of the outboard portion of the wing to allow the test to be performed in this test facility did not significantly affect the wing-nacelle interference phenomena since the nacelle was in a relatively inboard location in the present investigation. The chord line of the wing root was inclined at an incidence angle of 4.5° with a linear variation of twist distribution from the root to the 76.38-centimeter span station where the angle of incidence is approximately 2.5° . The twist varies linearly from this point to the 190.88-centimeter span station of the extended wing where the tip incidence is -1.75° . The model wing was constructed of aluminum by using the airfoil coordinates presented in table I(a).

Fuselage.- The fuselage has an elliptical nose, a cylindrical midsection, and a boat-tail afterbody. Coordinates of the fuselage are given in table I(b). The nose and afterbody of the fuselage were constructed of wood and the midsection was constructed of sheet aluminum.

Engine-pylon.- A cross-sectional view of the power fan-jet engine used in this investigation is shown in figure 4. The two-stage model fan is connected directly to a three-stage turbine which is driven by compressed gas. The model engine simulates the output of an actual engine with a bypass ratio of 8 and a fan-exit total-pressure ratio of 1.47 at the model-engine design maximum rotational speed of approximately 44 000 rpm.

Tests were conducted with the engine located in each of the five longitudinal and vertical positions shown in figure 5. Coordinates for the typical pylon are given in table I(c). The pylons were built in three sections: a removable aluminum leading-edge fairing, a steel core, and a removable aluminum trailing-edge fairing.

The powered model fan-jet engine, installed on an elongated pylon designed specially for obtaining engine-alone data, is shown in figure 6.

Driving-Gas System

The temperature of the model-engine driving fluid is reduced through expansion in the turbine to approximately 172° K. This fluid, therefore, must be virtually free of moisture to prevent formation of ice in the turbine and primary exit. A source of clean, very dry, high-pressure air was not available; therefore, nitrogen, a convenient, economical substitute for dry air, was used. Liquid nitrogen was gasified and piped through the wing and pylon to the engine. The gaseous nitrogen was preheated to approximately

293⁰ K before entering the model to reduce any thermal stress in the balance which might result from the close proximity of the nitrogen path to the balance.

The introduction of nitrogen into the wind-tunnel flow is considered to have little or no effect on the stream characteristics because of the similarity in the physical characteristics of nitrogen and air. The nitrogen control system consisted of an electrically operated dome regulator used as an engine speed control, a quick shutoff valve downstream of the regulator, and a pop-off valve installed as a final safety precaution to prevent the engine from exceeding its design rotational speed.

Instrumentation

Force balance.- Measurements of forces and moments were obtained from an internally mounted, wall-supported, five-component, electrical strain-gage balance. The model was designed so that the wing attached to the balance, but not to the fuselage, and protruded through a clearance opening in the fuselage. The fuselage, even though grounded to the tunnel wall, was attached to the balance wall-support system which allowed the fuselage to traverse through the angle-of-attack range.

Since part of the fuselage was submerged in the tunnel boundary layer, fuselage force measurements would be of no value. The effect of the fuselage flow field on the wing, pylon, and engine-nacelle forces, however, was present. Since the fuselage is cylindrical in the longitudinal region of these components, the effect these components would have on the forces of the fuselage should be relatively small.

Surface pressure measurements.- Wing chordwise pressure measurements were made on the upper surface near the wing-pylon juncture and on the lower surface approximately 4 centimeters to either side of the pylon. Longitudinal rows of pressure orifices on the surface of the engine were located at the 30⁰, 90⁰, 180⁰, 270⁰, and 330⁰ circumferential positions on the fan cowl; at the 30⁰, 60⁰, 90⁰, 180⁰, 270⁰, 300⁰, and 330⁰ circumferential positions on the turbine cowl; and at the 90⁰ and 270⁰ circumferential positions on the turbine plug. Longitudinal locations of the pressure orifices are presented in table II.

Engine internal pressure measurements.- Stagnation and static pressures in the fan inlet and exit and at the turbine inlet and exit were measured for use in computing engine thrust. The fan-inlet stagnation pressure was measured by two total-pressure rakes consisting of six pressure probes each. Both rakes were located just forward of the first-stage fan rotor - one rake at the 22⁰ circumferential position and the other at the 180⁰ position. (See fig. 4.) The space between rake probes was decreased in the vicinity of the fan-inlet wall to measure any change in the boundary layer resulting from the various flow conditions. The height of the rakes from the inlet wall to the fan hub was limited by

rake vibration resulting from the close proximity of the rake to the first-stage fan blades. The individual rake-probe pressure measurements were area weighted before being used in the thrust computations.

Two static-pressure orifices were employed at the 14° and 188° positions in the plane of the fan-inlet rakes to measure the static pressure in the vicinity of the total-pressure rakes. An 8° spacing between the static-pressure orifice and the total-pressure rake was used to reduce interference in the static pressure resulting from the presence of the rake.

The fan-exit instrumentation consisted of seven total-pressure rakes located circumferentially approximately every 51° . Each total-pressure rake had five probes spaced radially in such a manner that each probe was centered in one of the five concentric circular equal-area segments into which the exit area had been divided. These areas were then equally divided circumferentially among the seven rakes to provide an equal weighing factor for each probe. The total-pressure rake at the 0° position also supported six thermocouple probes. One thermocouple was located between each pressure probe and between the pressure probes at the extreme ends of the rake and the engine surface.

Seven static-pressure orifices were located on the turbine cowl surface just inside the fan exit at the 30° , 60° , 90° , 180° , 270° , 300° , and 330° positions.

The flow condition at the turbine exit was measured by two total-pressure rakes located at the 60° and 300° positions and with two static-pressure orifices located on the turbine-plug surface just inside the turbine exit at the 90° and 270° positions.

All wing-pressure measurements, as well as the engine internal- and external-pressure measurements, were made by six pressure-scanning valves mounted inside the fuselage. Each valve was capable of measuring 47 pressures by an internal strain-gage transducer plus a reference pressure.

Calibration of model engine.- Because of the inadequacy of the flow-survey instrumentation used in the fan inlet and exit, a fan-flow calibration was required. The ASME flow nozzle shown in figure 7 was used for this calibration. The actual engine mass flow could be determined from the static-pressure measurements in the constant-area portion of the ASME flow nozzle, the ambient stagnation pressure and temperature, and the nozzle flow coefficient of 0.995. This measured mass-flow value was then divided by the mass flow calculated from the measurements made in the fan inlet. The resulting flow coefficient was used to correct the inlet mass-flow measurements made during the investigation.

Test Conditions

Investigations were made of the complete wing-fuselage-pylon-engine configuration, of the wing-fuselage-pylon configuration, of the wing-fuselage configuration, and of the

engine-alone configuration. The engine-alone configuration was mounted on the elongated pylon which was attached directly to the wall-mounted force balance. Data for this configuration were obtained at an angle of attack of 0° only.

The tunnel total pressure was reduced to 0.87 atmosphere (88.2 kN/m^2) throughout the entire investigation because of the operating limits of the model engine and the nitrogen-supply valving system. The tunnel stagnation temperature was reduced from the tunnel normal operating temperature of 322° K to 311° K to match as closely as possible the temperature of the incoming nitrogen. A further reduction in tunnel temperature resulted in unacceptable icing conditions on the rear portion of the turbine cowl and turbine plug. The tunnel dewpoint temperature of approximately 250° K was maintained throughout the investigation in an attempt to reduce engine icing as much as possible.

Tests were conducted at Mach numbers of 0.70, 0.78, 0.81, and 0.84 and over an angle-of-attack range of 0° to 4° (engine-alone configuration tested only at $\alpha = 0^\circ$), which resulted in a range of lift coefficient above and below that required for cruise flight for this type of airplane. The Reynolds number range based on the wing mean geometric chord \bar{c} of 58.30 centimeters was from 6.67×10^6 to 7.38×10^6 .

The engine was operated at fan-exit total-pressure ratios of 1.00 and 1.47. The fan-exit total-pressure ratio of 1.00 was obtained with the engine operating just fast enough (approximately 23 000 rpm) to overcome the internal losses of the engine, and zero fan thrust was produced. A fan-exit total-pressure ratio of 1.47 was obtained with the engine operating at the maximum design speed (44 000 rpm), and maximum thrust was produced.

For all tests, boundary-layer transition strips, 0.32 centimeter wide and consisting of No. 120 carborundum grains, were installed on the upper and low wing surfaces and on the pylons at the 10-percent-local-chord location. Transition strips were also fixed on the fan cowl at a streamwise location 1.27 centimeters from the inlet leading edge both on the inside and outside of the inlet.

INTERFERENCE DRAG

To obtain the value of only the interference drag resulting from the effect of the pylon-engine combination in the presence of the wing including the effect of the power engine wake, the total drag measured by the force balance is reduced by the computed thrust and by the drag of the three individual components of the model: wing, engine, and pylon. This procedure is shown by the following equation:

$$\Delta C_D = (C_D)_{\text{complete model}} - (C_D)_{\text{wing}} - (C_D)_{\text{engine}} - (C_{D,f})_{\text{pylon}}$$

where

$$(C_D)_{\text{complete model}} = (C_D)_{\text{bal}} + C_{F,n}$$

$(C_D)_{\text{bal}}$ total measured wing-pylon-engine drag coefficient, based on reference wing area of 0.776 meter², obtained from wall-mounted strain-gage force balance

$C_{F,n}$ engine net-thrust coefficient computed as shown in appendix

$(C_D)_{\text{wing}}$ wing drag coefficient, obtained from wall-mounted strain-gage force balance during tests made with engine and pylon removed

$$(C_D)_{\text{engine}} = (C_D)_{\text{bal}} + C_{F,n} - (C_D)_{\text{pylon}}$$

$(C_D)_{\text{bal}}$ measured drag coefficient obtained from engine alone mounted on elongated pylon, at 0° angle of attack only

$C_{F,n}$ engine-alone net-thrust coefficient computed as shown in appendix

$(C_D)_{\text{pylon}}$ drag coefficient of elongated pylon alone

$(C_{D,f})_{\text{pylon}}$ skin-friction drag coefficient of pylon used with wing-engine-fuselage combination

VALIDITY OF RESULTS

The absolute force measurements made during this investigation are of little value for the following reasons: The fuselage of the test model was not attached to the balance, only the inner portion of the original wing was used, and there was a gap drag associated with the wing protruding through the clearance opening in the fuselage. Furthermore, because of the limitations of the instrumentation, the computed thrust values are not considered reliable as absolute values. Therefore, most of the absolute results of the investigation are not presented herein. The drag results for the basic wing-alone configuration are presented in figure 8 to indicate the compressibility drag rise characteristics of this test configuration.

The analysis presented is based on the differential values of the data obtained as described in the preceding section entitled "Interference Drag." The validity of these increments is considerably greater than that of the absolute results. Any systematic inaccuracies in drag measured by force balance tend to cancel when the drag of the complete configuration is reduced by the measured drag of the wing-alone configuration. Also, the systematic errors in computing thrust tend to cancel since the thrust of the complete configuration is added to the total balance-drag value whereas the thrust for the engine-alone configuration is subtracted. However, even these incremental results are subject to the following qualifications:

The data for the engine-alone configuration were obtained through the Mach number range of 0.70 to 0.84 at an angle of attack of 0° only. These data when applied to the interference drag computation at angles of attack other than 0° introduce a slight error. Unpublished data obtained for a similar engine-alone configuration indicate that this error is negligible through the cruise angle-of-attack range up to approximately 2° and increased appreciably with a further increase in angle of attack. The interference-drag results presented herein for an angle of attack of 4° are therefore questionable but are conservative inasmuch as the error involved tends to make the interference drag (ΔC_D) slightly more positive.

An additional error is introduced by the upward inclination of the thrust vector at angles of attack greater than 0° . Such an inclination increases the lift and reduces the thrust measured by the balance. An analysis of the effect of such changes suggests that at angles of attack near that for cruise, this upward inclination results in a decrease of approximately 0.0001 in the interference-drag coefficients presented herein. At the highest test angle of attack of 4° , an increase of approximately 0.0002 in the interference-drag coefficients occurs.

The results presented are also subject to random errors that possibly exist in the force-balance measurements and computed thrust.

In spite of the foregoing qualifications, however, the results presented are considered sufficiently reliable to be indicative of the general interference phenomenon that exists for the engine-pylon-wing combination. This conclusion is supported by the fact that unpublished results of a similar investigation with more refined instrumentation indicate trends similar to those presented herein.

RESULTS AND DISCUSSION

Cruise Condition

Pylon end-plate effect.- The interference-drag coefficient (ΔC_D) resulting from changing the engine positions is presented in figure 9 as a function of Mach number at

the cruise lift coefficient of 0.4. Favorable aerodynamic interference ($-\Delta C_D$) is obtained for each engine position investigated at and below the cruise Mach number of 0.78. An increase in favorable interference occurs in this Mach number range as a result of the addition of power for all configurations except the pylon 1 configuration. The greatest favorable interference is obtained with pylon 4 where the engine is in its most forward and vertically lowest position, approximating the engine location used in the design of the latest cargo aircraft.

The variation of the aerodynamic-drag coefficient with lift coefficient at each test Mach number for the five pylon configurations is presented in figure 10. The interference-drag data obtained for pylon 4 (see fig. 10(d)) show that at $M = 0.78$ there is no favorable interference obtained at the lowest test lift coefficient but there is an increase in favorable interference associated with an increase in lift coefficients for the maximum thrust case, the maximum favorable interference occurring at the highest test lift coefficient shown. This variation suggests that the measured favorable interference might result from a reduction of induced drag caused by an end-plate effect of the pylon and nacelle. Such a reduction of induced drag by an underwing inboard end-plate effect has been predicted theoretically (ref. 2).

To provide this reduction in induced drag, the pylon-nacelle combination must reduce the outward, spanwise flow under the wing. Associated with such an effect, there must be an outward side force on the pylon-nacelle combination. Pressure distributions similar to those presented in figure 11 are used to obtain the differential pressure coefficients shown plotted in figure 12 against longitudinal distance from the wing leading edge for $M = 0.78$. The differences in the pressures measured on the engine just outboard and inboard of the pylon are indicative of the force that exists on the pylon near the engine. The differential pressures presented in figure 13, obtained from wing lower-surface pressures measured on either side of the pylon (see fig. 11), also indicate the probable pylon forces in this region. Both figures 12 and 13 show an increase in outward side force on the pylon with an increase in angle of attack. This force results from an inclination of the pylon-nacelle with respect to local flow under the wing.

This pylon-nacelle outward side force, when resolved with respect to the local flow, has a forward inclination relative to the flight path rather than the usual rearward or drag direction. This action is the primary factor resulting in the favorable-interference-drag decrement measured by the force balance.

Power effect.- The effect of power can be seen from the differential pressure coefficients at the engine-pylon juncture by comparing the results obtained for a fan-exit total-pressure ratio of 1.00 with that obtained for a fan-exit total-pressure ratio of 1.47 at the cruise Mach number. (See fig. 12.) Considerably greater side force is produced by the pylon at the maximum-thrust conditions than with the engine operating at a pressure ratio

of 1.00. The pylon section force coefficient, obtained by an integration of pressures of figure 12 indicates that this force, in the side-force direction, is approximately doubled as a result of the addition of power. A possible explanation for this effect of power on pylon lift is that with the engine operating at the zero-thrust condition there is a tendency for the higher pressure on the inboard side of the pylon to propagate upstream through the subsonic fan flow and around the internal leading edge of the pylon. This pressure leakage raises the lower pressure associated with the high-velocity flow on the outboard surface of the pylon. This reduction of pylon differential pressure results in a reduced favorable aerodynamic interference. When the engine is producing maximum thrust, the fan exit is choked and this pressure leakage can no longer occur; hence, more effective end-plate action can be derived from the engine.

From the differential pressure coefficients obtained at the wing-pylon juncture (fig. 13), it may be seen that there is essentially no effect of power in the region of the wing-pylon juncture. This fact would indicate that any improvement resulting from the addition of power will be realized only locally.

Off-Design Conditions

Effect of engine position.- Although there is a decrease in the interference associated with an increase in lift coefficient for almost all engine positions investigated (see fig. 10), there is a shift in the level of the variation of aerodynamic interference with lift for the various engine positions. For example, a marked increase in the level of interference is associated with the rearward and the vertically upward movement of the engine from the most favorable design position (pylon 4) to the least favorable position investigated (pylon 3). This increase is the result of a loss in pylon side force associated with the engine position change. A possible reason for the lift reduction is suggested by the variation in the pressure coefficients on the inboard surface of these two pylons at the wing-pylon juncture and at the engine-pylon juncture. These data (see fig. 14) indicate an increase in velocity on the inboard side of the pylon under the forward part of the wing associated with the change in engine position. This change probably results from an increase in the aerodynamic blockage between the engine, the pylon, the wing, and the fuselage associated with the upward and rearward movement of the engine-pylon configuration.

Effect of Mach number.- The adverse effect on aerodynamic interference resulting from an increase in Mach number above the cruise Mach number of 0.78, previously shown in figures 9 and 10, is possibly caused by shock formations and associated separation resulting from higher local Mach number; however, such changes are not indicated by the pressure distribution on the engine or on the wing near the pylon. Even the pressure distribution for the most suspect region inboard of the pylon (see fig. 15) indicates no such problem.

CONCLUSIONS

The results of the present experimental investigation to determine the effect of engine installation on the aerodynamic interference of a semispan model of a transport airplane configuration, including the effect of the fan-jet wake, indicate the following conclusions:

1. The interference drag, that is, the difference between the drag for the complete configuration and the sum of the drags of the components, may be favorable for an underwing engine-pylon installation on the type of aircraft simulated during this investigation at the design cruise lift coefficient and Mach number.

2. Pressure measurements obtained from the engine and wing surfaces in the vicinity of the pylon suggest that the favorable interference obtained during this investigation may be due to a reduction in induced drag associated with an inboard end-plate effect of the pylon and nacelle.

3. The addition of engine power has a strong influence on the aerodynamic interference. For the design engine position, the favorable interference for maximum power was double that for the power-off case.

4. The longitudinal and vertical position of the engine has a pronounced effect on interference drag. The greatest favorable interference was obtained during this investigation with the engine in the most forward longitudinal and lowest vertical test position.

5. An increase in Mach number above the design cruise speed has an adverse influence on the aerodynamic interference.

Langley Research Center,
National Aeronautics and Space Administration,
Langley Station, Hampton, Va., February 29, 1968,
126-13-01-32-23.

APPENDIX

COMPUTATIONS

Forces

The forces, measured by the force balance, have been reduced to lift and drag coefficients by using the semispan wing area of 0.776 meter².

Thrust

The net thrust of the model engine has been defined as the momentum change through the fan, the additional momentum of the nitrogen exhausted from the primary exit, less the scrubbing drag resulting from the fan- and primary-exit flows:

$$F_n = F_{g,f} - D_r + F_{g,p} - D_s \quad (A1)$$

Fan gross thrust.- The fan gross thrust has been computed as the product of the fan mass flow and the average fan-exit velocity, plus the fan-exit pressure force:

$$F_{g,f} = \dot{m}_i (V_e)_{av} + [(p_e)_{av} - p_\infty] A_e \quad (A2)$$

In computing the fan gross thrust, the mass flow determined at the fan inlet has been used rather than the mass flow measured at the exit because of the smaller variation in mass-flow correction $K_{m,i}$ with the various test conditions. It is probable that this procedure gives more reliable results. The mass flow is computed in the following manner:

$$\dot{m}_i = [\rho_i (V_i)_{av} A_i] K_{m,i} \quad (A3)$$

The density is computed from the thermal equation of state as follows:

$$\rho_i = \frac{(p_i)_{av}}{R (T_{s,i})_{av}} \quad (A4)$$

The average inlet static pressure was obtained from the fan-inlet measurements. The local static temperature was determined from the measured stream total temperature and the average inlet Mach number as follows:

$$(T_{s,i})_{av} = \frac{T_{t,\infty}}{1 + \frac{\gamma - 1}{2} [(M_i)_{av}]^2} \quad (A5)$$

APPENDIX

The inlet Mach number was computed in the conventional manner from the weighted average inlet total-pressure and static-pressure measurements.

The average fan-inlet velocity is computed as follows:

$$(V_i)_{av} = (M_i)_{av} \sqrt{\gamma R (T_{s,i})_{av}} \quad (A6)$$

The required fan-exit velocity is determined in a similar manner to that used for the inlet velocity based on the total-pressure and static-pressure measurements made at the fan exit; that is,

$$(V_e)_{av} = (M_e)_{av} \sqrt{\gamma R (T_{s,e})_{av}} \left(\frac{\dot{m}_i}{\dot{m}_e} \right) \quad (A7)$$

The exit Mach number is computed from the average total-pressure measurements made at the fan exit and the average exit static pressures measured on the turbine cowl, located just inside of the fan exit. The average exit static pressure was adjusted by a calibration constant established from a fan-exit static-pressure survey made during an initial engine calibration to give a mean static pressure across the fan exit. The fan-exit static temperature is computed from the average total temperature measured in the fan exit by using the preceding static-temperature equation (eq. (A5)).

The exit velocity determined by these calculations must be corrected by a factor similar to that needed for mass flow. Just as for the exit mass-flow factor, this correction varies with test conditions; thus, it cannot be determined from a static calibration. An analysis of the factors influencing this correction indicates that possible errors in the static pressures have little effect on the exit velocity and that the greatest effect is due to the incompleteness of the total-pressure measurements, in particular to the lack of total-pressure measurements in the boundary layer at the exit. With the assumption that the errors are due primarily to exit total-pressure measurements, then the errors in the exit velocity are similar to the errors in mass flow, and the correction factor to be applied to the velocity is equal to the ratio of mass flow in the inlet to the apparent mass flow at the exit. Although such a correction is undoubtedly not exact, it has been used here in an attempt to obtain a first-order correction of the fan-exit velocity. The exit mass flow used in the ratio was determined in the same manner as the inlet mass flow based on exit measurements.

Ram drag.- The ram drag is the initial momentum of the air entering the fan inlet and is the product of the mass flow determined from inlet measurements and the stream velocity:

$$D_R = \dot{m}_i V_\infty \quad (A8)$$

APPENDIX

Primary thrust.- The primary gross thrust is obtained in a similar manner to that used to determine fan gross thrust:

$$F_{g,p} = \dot{m}_{p,e}(V_{p,e})_{av} + [(p_{p,e})_{av} - p_{\infty}]A_{p,e} \quad (A9)$$

No measurements of the turbine inlet mass flow were made; therefore, the measured turbine-exit mass flow was used in computing the primary thrust. Consequently, a correction must be applied to the primary thrust to account for the inadequacy in the determination of the exit mass flow and velocity. A constant correction of 0.953, which is a mean of the correction values applied to the fan thrust, is applied to the primary-thrust calculation. The primary-exit static pressure was also adjusted to give a mean pressure, as in the case of the fan, by a constant obtained from the initial engine calibration.

Scrubbing drag.- The thrust computations of the present test are reduced by the scrubbing drag. This skin-friction drag is obtained from the following equation:

$$D_s = c_f(A)_{wet}q \quad (A10)$$

The scrubbing drag is computed from equation (A10) by using the dynamic pressure and Reynolds number based on average local conditions on the fan cowl, fan-exit conditions on the turbine cowl, and primary-exit conditions on the turbine plug. The friction coefficient was obtained from the Sommer and Short T' method (ref. 3).

Thrust coefficient.- The thrust is reduced to coefficient form by using the stream dynamic pressure and the wing reference area in the following manner:

$$C_{F,n} = \frac{F_n}{qS} \quad (A11)$$

The thrust coefficient for the complete airplane configuration and that for the engine-alone configuration are used in the determination of the interference drag.

REFERENCES

1. Wright, Ray H.; Ritchie, Virgil S.; and Pearson, Albin O.: Characteristics of the Langley 8-Foot Transonic Tunnel With Slotted Test Section. NACA Rep. 1389, 1958. (Supersedes NACA RM L51H10 by Wright and Ritchie and RM L51K14 by Ritchie and Pearson.)
2. Mangler, W. (G. de Montalvo, trans.): Lift Distribution on Wings With Lateral Plates. DAC Rep. No. 33497, Douglas Aircraft Div., Dec. 2, 1966.
3. Sommer, Simon C.; and Short, Barbara J.: Free-Flight Measurements of Turbulent-Boundary-Layer Skin Friction in the Presence of Severe Aerodynamic Heating at Mach Numbers From 2.8 to 7.0. NACA TN 3391, 1955.

TABLE I.- WING, FUSELAGE, AND PYLON COORDINATES

(a) Wing airfoil ordinates

[Stations and ordinates in percent wing mean geometric chord]

Station	Ordinate	
	Upper surface	Lower surface
	Wing root; $i_w = 4.5^\circ$	
0	10.3	10.3
.1	10.6	9.9
.1	10.8	9.8
.3	11.1	9.5
.7	11.4	9.2
1.0	11.6	9.0
1.6	12.0	8.6
3.3	12.6	7.7
6.6	13.6	6.4
9.9	14.2	5.3
13.2	14.5	4.3
16.4	14.7	3.4
19.7	14.7	2.6
23.0	14.8	1.8
26.3	14.7	1.2
32.9	14.6	0
39.5	14.2	-9
52.6	13.3	-2.1
65.8	11.9	-2.7
76.3	10.7	-2.7
79.0	10.3	-2.7
92.1	8.4	-2.3
105.3	5.9	-1.6
118.4	3.1	-.8
131.6	0	0
	$y = 76.38 \text{ cm}; i_w = 2.5^\circ$	
0	4.0	4.0
0	4.3	3.6
.1	4.4	3.5
.2	4.7	3.3
.5	5.0	3.1
.7	5.2	2.9
1.2	5.6	2.7
2.3	6.4	2.3
4.6	7.4	1.8
6.9	8.1	1.4
9.2	8.5	1.1
11.4	8.8	0.7
13.7	9.0	.5
16.0	9.2	.3
18.3	9.3	0
22.9	9.3	-.2
27.5	9.2	-.2
36.6	8.9	-.6
45.8	8.2	-.7
53.1	7.4	-.7
55.0	7.2	-.7
64.1	5.7	-.6
73.3	3.9	-.4
82.4	2.0	-.2
91.6	0	0
	$y = 190.88 \text{ cm}; i_w = -1.75^\circ$	
0	-1.0	-1.0
0	-.9	-1.1
0	-.8	-1.1
.1	-.7	-1.2
.2	-.6	-1.3
.2	-.5	-1.3
.4	-.4	-1.4
.8	-.1	-1.5
1.6	.3	-1.6
2.4	.6	-1.7
3.2	.8	-1.7
4.0	1.0	-1.8
4.9	1.1	-1.8
5.7	1.2	-1.8
6.5	1.3	-1.8
8.1	1.5	-1.8
9.8	1.6	-1.7
13.0	1.7	-1.5
16.3	1.7	-1.3
18.9	1.6	-1.0
19.6	1.6	-1.0
22.9	1.3	-.7
26.1	.9	-.5
29.4	.4	-.3
32.7	0	0

TABLE I.- WING, FUSELAGE, AND PYLON COORDINATES - Continued

(b) Fuselage coordinates

[Stations and ordinates in percent fuselage length]

Station	Ordinate
0	0
.4	1.4
.8	2.0
1.2	2.4
1.6	2.8
2.0	3.1
2.4	3.4
2.8	3.6
3.2	3.9
6.3	5.1
7.9	5.5
9.5	5.8
11.1	6.0
12.7	6.1
14.3	6.2
65.9	6.2
68.3	6.1
70.2	6.1
72.2	6.0
74.2	5.8
76.2	5.6
78.2	5.3
80.2	5.0
82.1	4.7
84.2	4.3
88.1	3.4
100.0	.5

TABLE I.- WING, FUSELAGE, AND PYLON COORDINATES - Concluded

(c) Typical pylon coordinates

[Stations and ordinates in percent wing mean geometric chord]

Station	Ordinate	
	Upper surface	Lower surface
0.3	0.3	-0.3
.6	.4	-.4
1.3	.5	-.5
1.9	.6	-.6
3.2	.8	-.8
6.5	1.1	-1.1
13.0	1.6	-1.6
19.4	1.8	-1.8
25.9	1.9	-1.9
32.4	1.9	-1.9
38.9	1.8	-1.8
45.4	1.4	-1.4
51.9	1.0	-1.0
58.3	.5	-.5
64.8	.1	-.1

TABLE II.- PRESSURE-ORIFICE LOCATIONS

(a) Wing pressure orifices

[Stations in percent of local wing chord]

Station on -		
Upper surface y = 52.45 cm (Local chord is 60.07 cm)	Lower surface y = 51.05 cm (Local chord is 61.09 cm)	Lower surface y = 58.67 cm (Local chord is 58.78 cm)
1	1	1
2	2	2
4	4	4
7	7	7
10	10	10
15	15	20
20	20	25
30	25	30
40	30	35
50	35	40
60	40	50
70	45	
80	50	
90	60	
100		

TABLE II.- PRESSURE-ORIFICE LOCATIONS – Concluded

(b) Engine pressure orifice, pylon 4 configuration

[Station in percent chord at wing-pylon juncture]

Station* on –		
Fan cowl	Turbine cowl	Plug
-61.2	-22.6	10.2
-61.1	-19.7	11.9
-60.8	-14.8	14.3
-59.7	-11.1	16.0
-58.5	-7.8	18.1
-56.6	-4.6	20.4
-54.7	-1.9	
-51.6	0.7	
-45.6	3.7	
-37.4	6.6	
-30.4	8.9	
-27.0	10.2	
-22.6		

*Measured from leading edge at wing-pylon juncture to the engine pressure orifices; $c = 60.07$ cm.

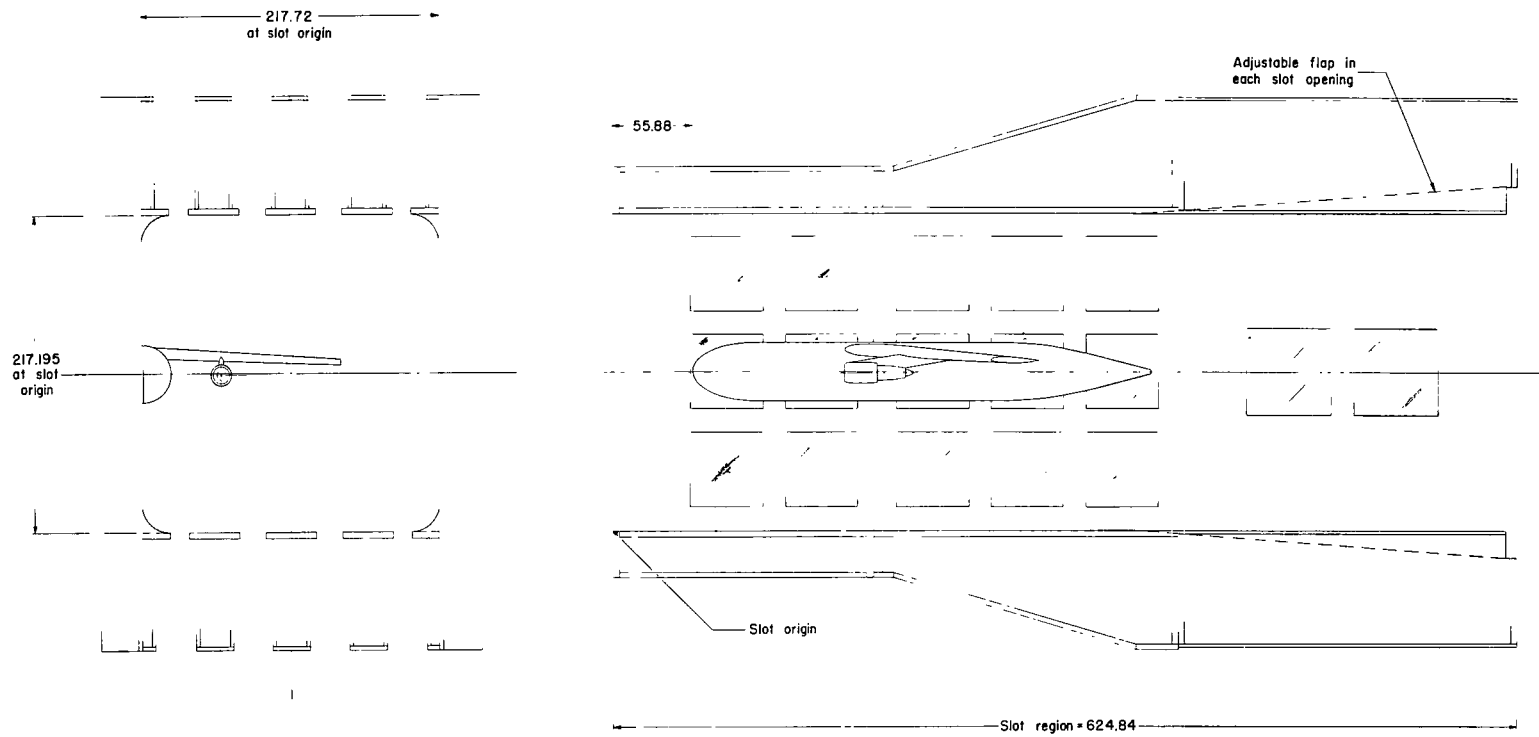
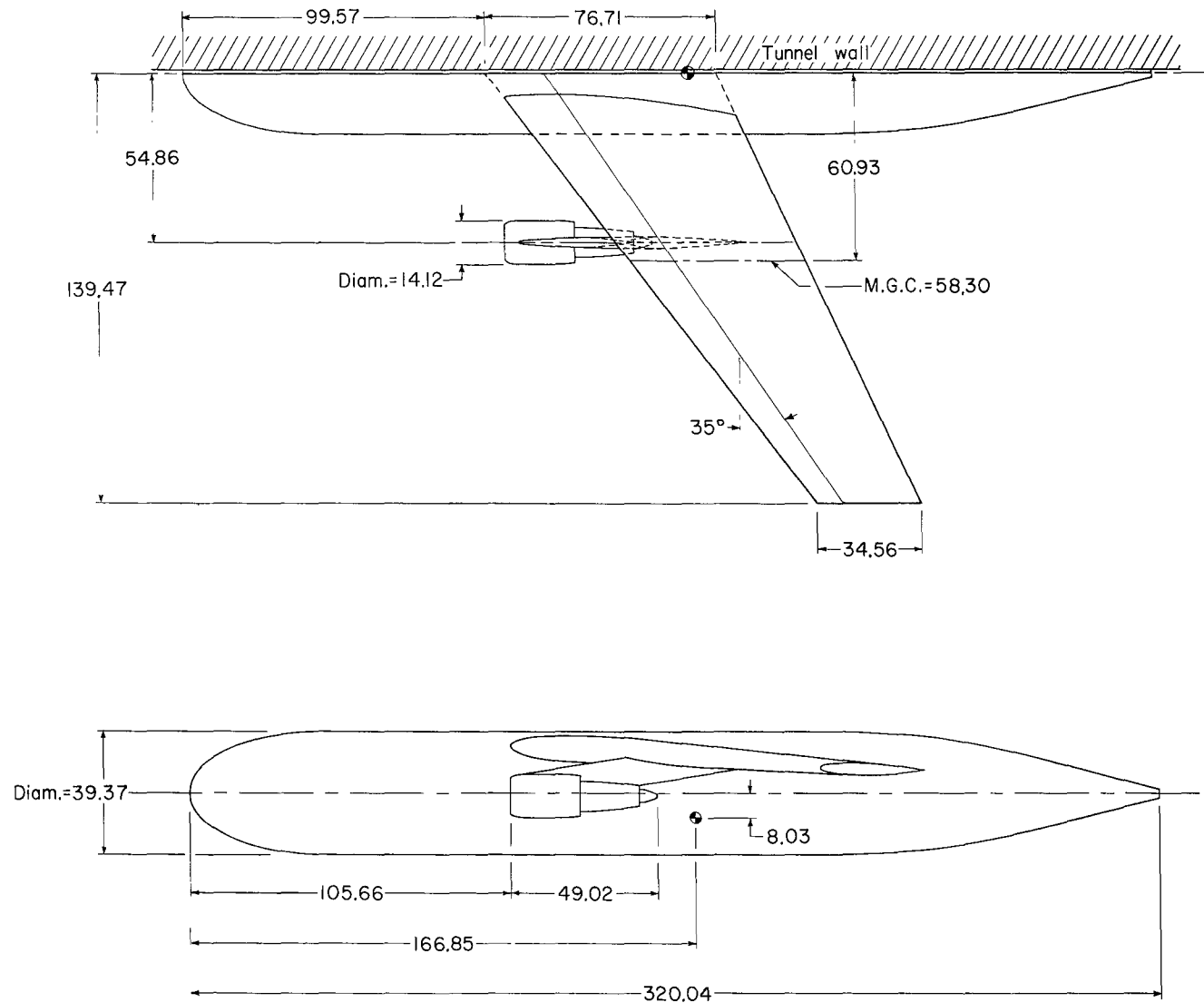
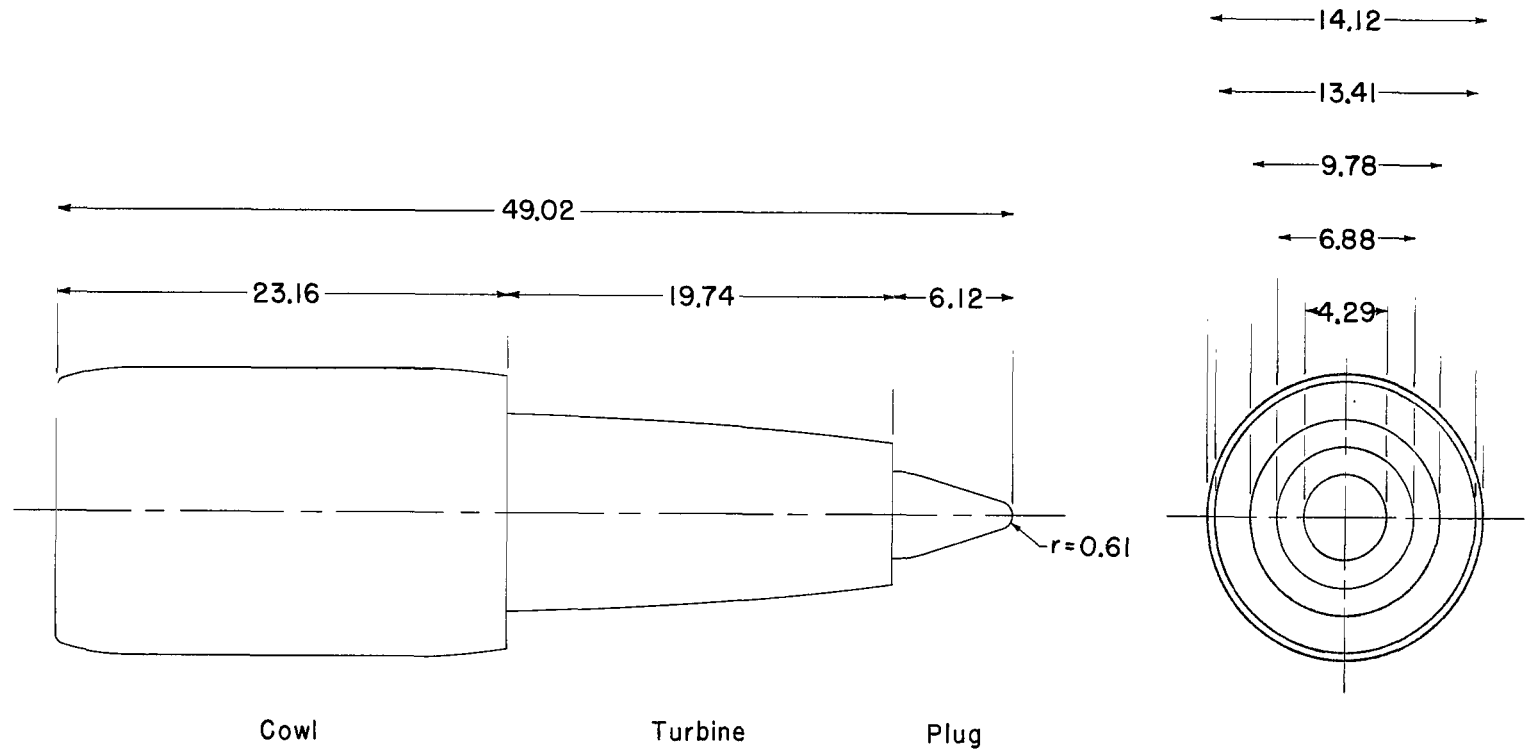


Figure 1.- Details of test section and location of model in the Langley 8-foot transonic pressure tunnel. All dimensions are in centimeters.



(a) Details of test model.

Figure 2.- Drawing of the semispan transport model. All dimensions are in centimeters.



(b) Details of model engine.

Figure 2.- Concluded.

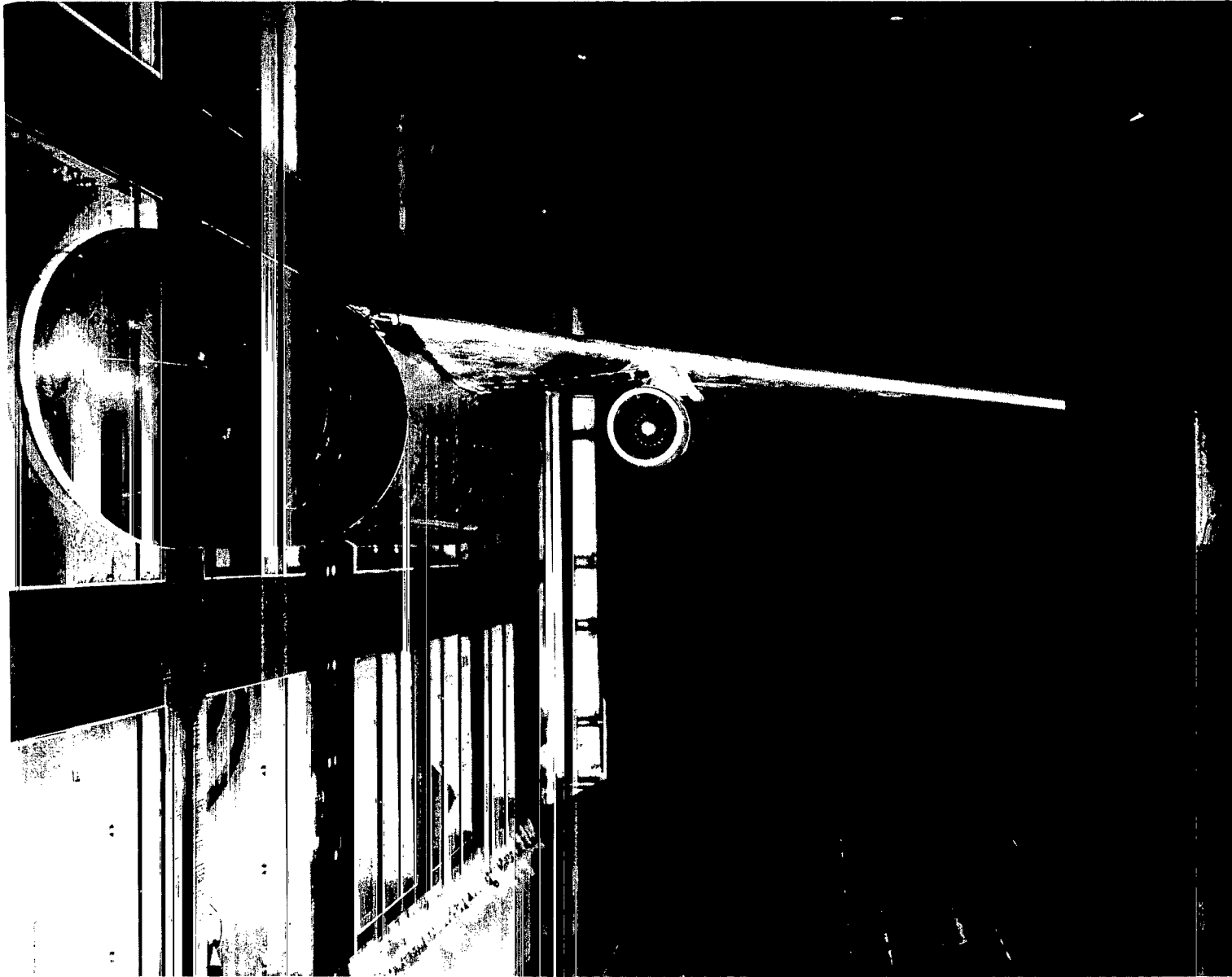


Figure 3.- Photograph of the semispan model mounted on the wall of the Langley 8-foot transonic pressure tunnel.

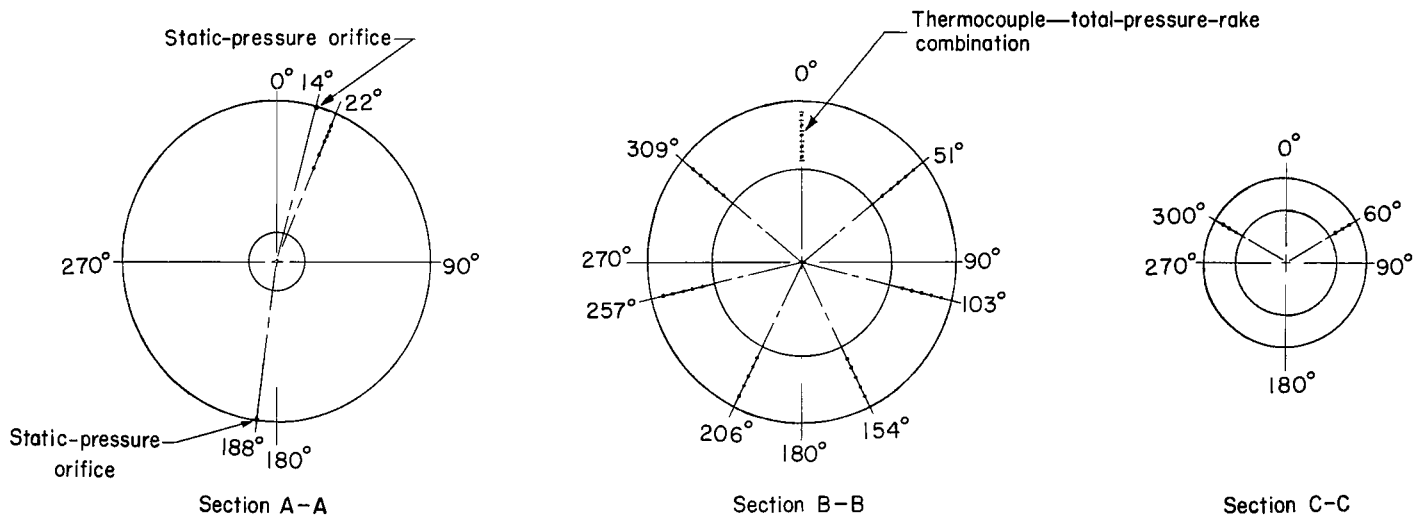
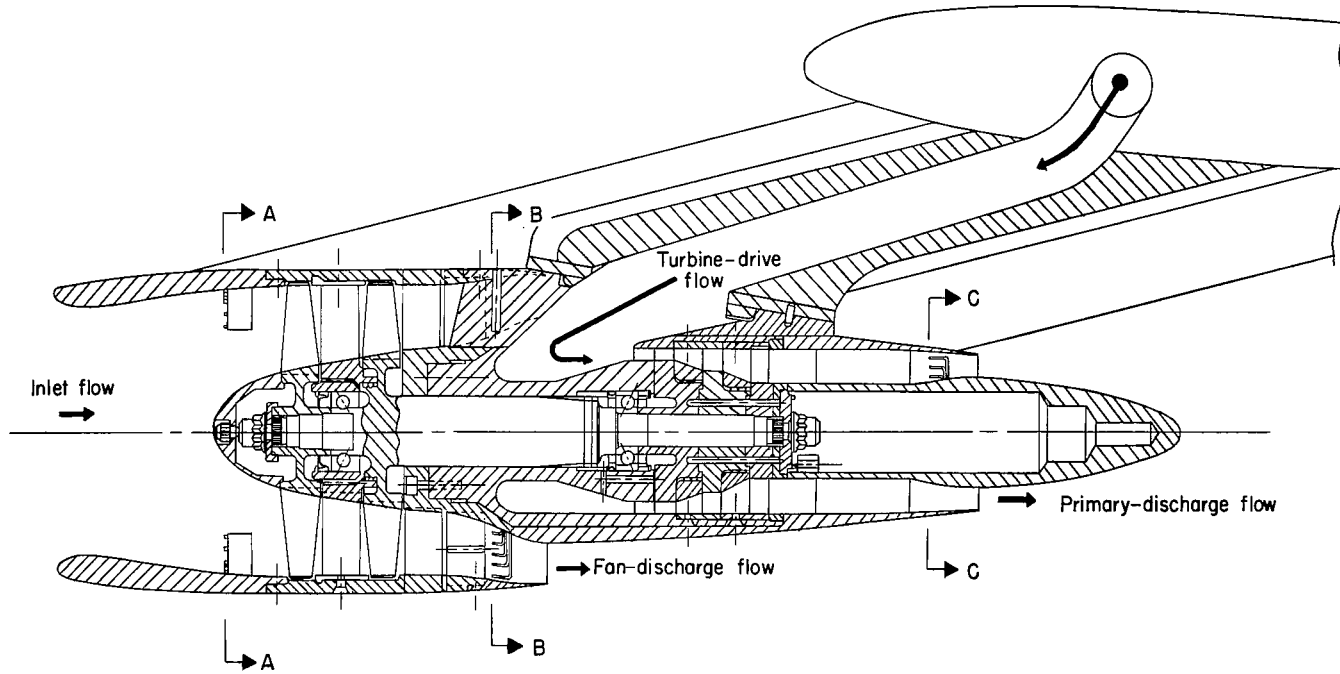
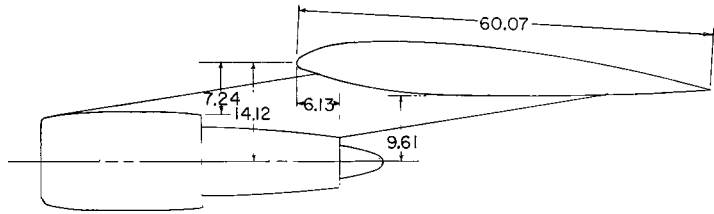
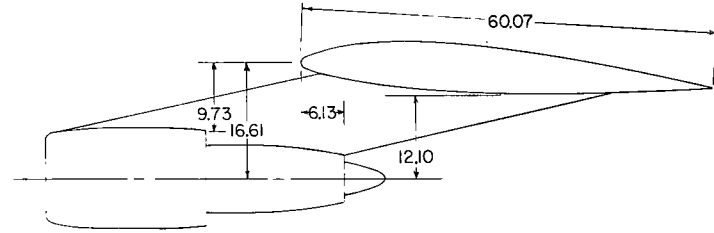


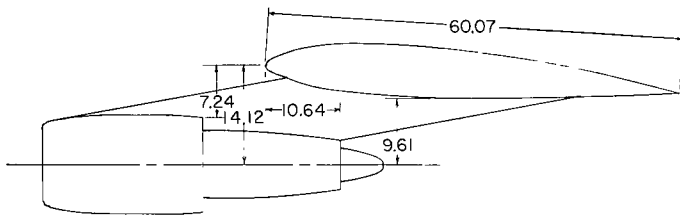
Figure 4.- Cross-sectional view of the powered model fan-jet engine.



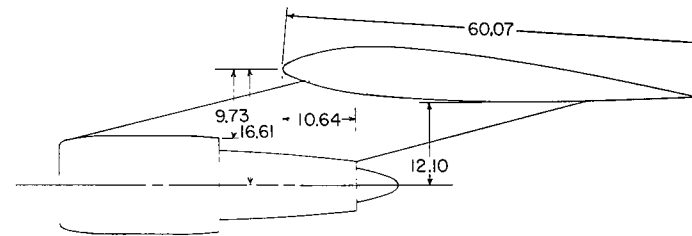
Pylon 1



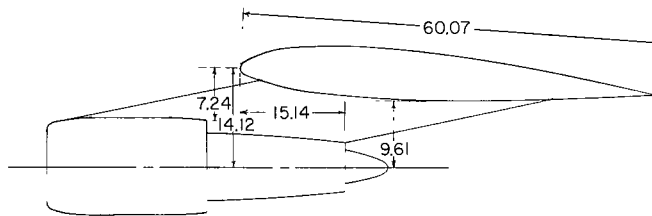
Pylon 4



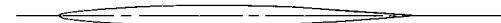
Pylon 2



Pylon 5



Pylon 3



Typical pylon section

Figure 5.- Details of engine positions. All dimensions are in centimeters.

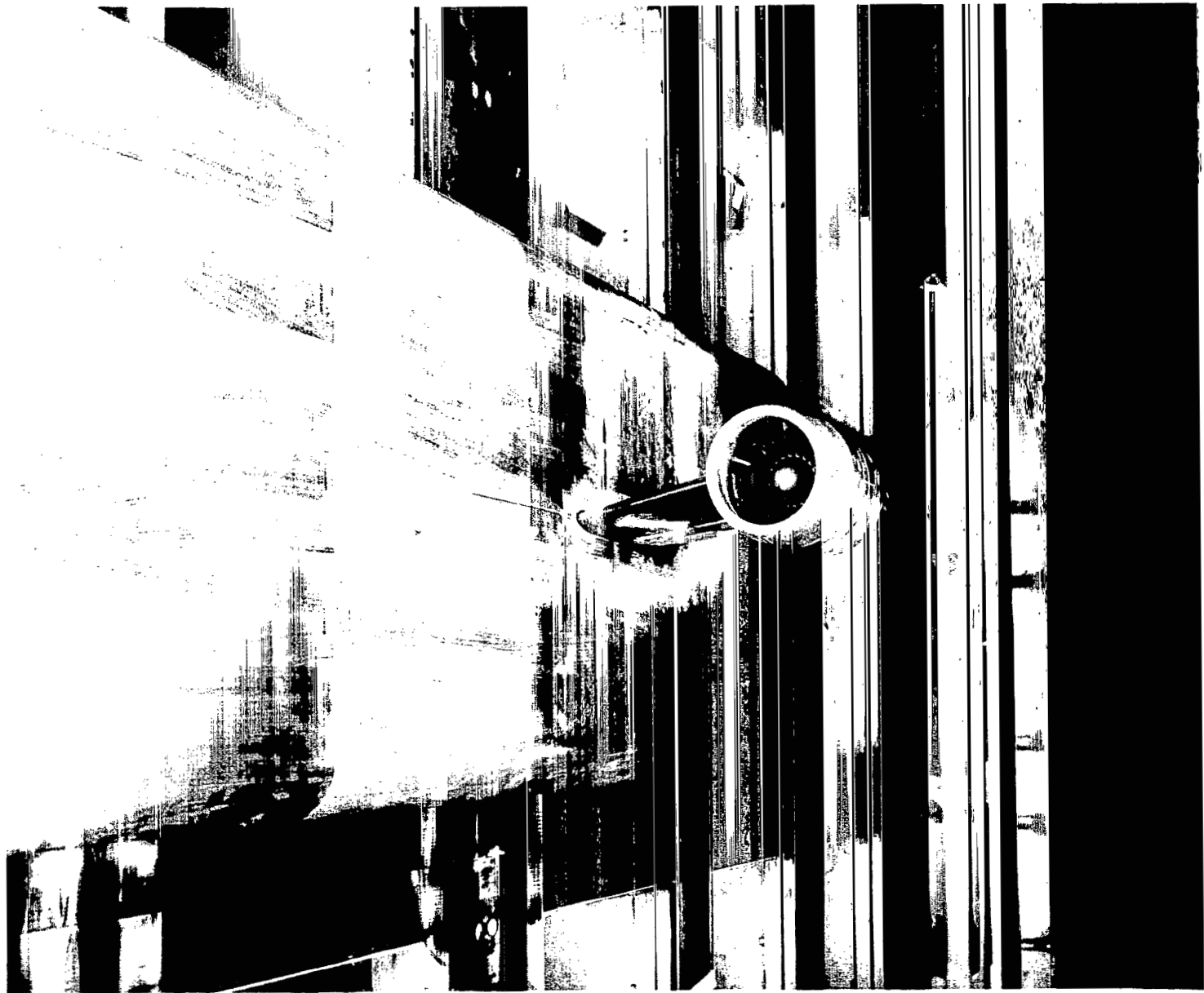


Figure 6.- Photograph of the model engine and elongated pylon wall mounted in the Langley 8-foot transonic pressure tunnel.

L-65-4643

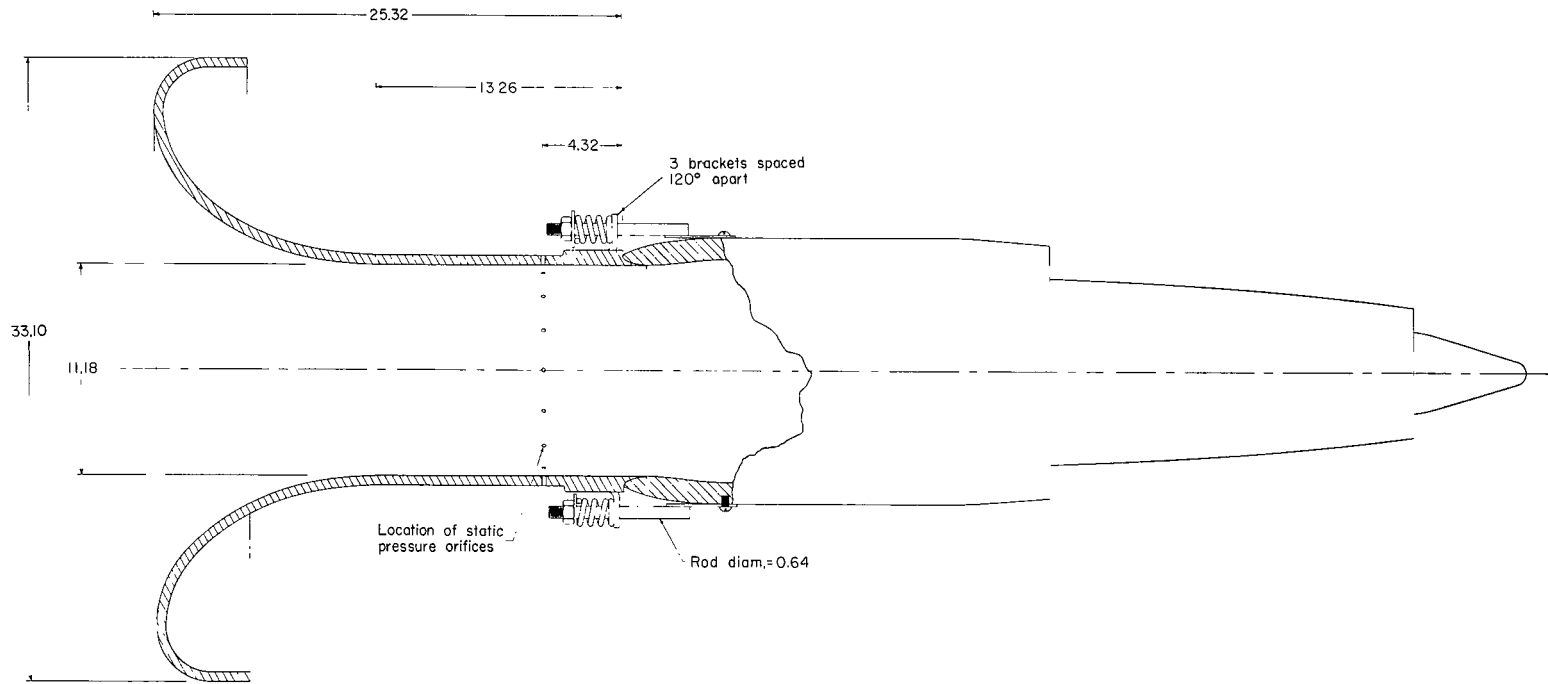
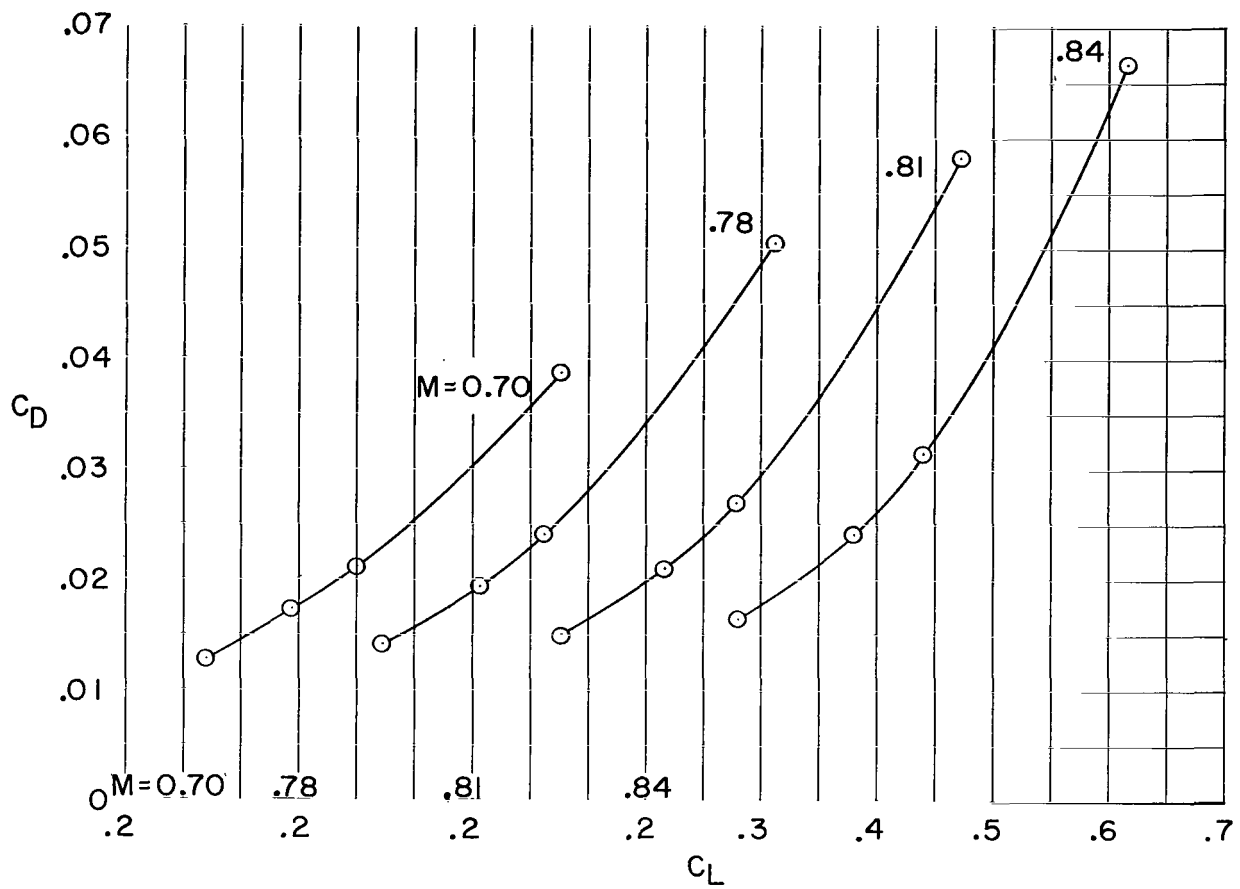
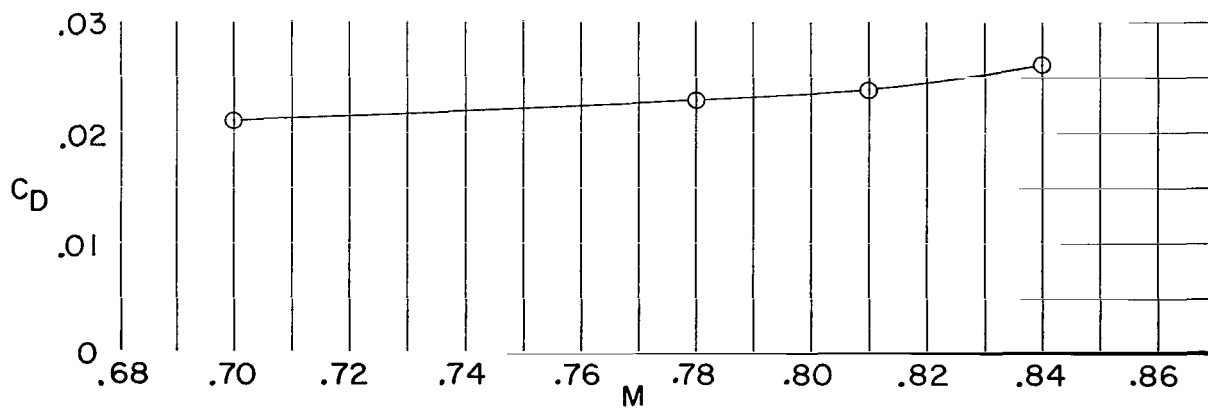


Figure 7.- Cross-sectional view of the ASME flow nozzle. All dimensions are in centimeters.



(a) Variation of drag coefficient with lift coefficient for various Mach numbers.



(b) Variation of drag coefficient with Mach number for a lift coefficient of 0.4.

Figure 8.- Drag characteristics of the wing in presence of the fuselage.

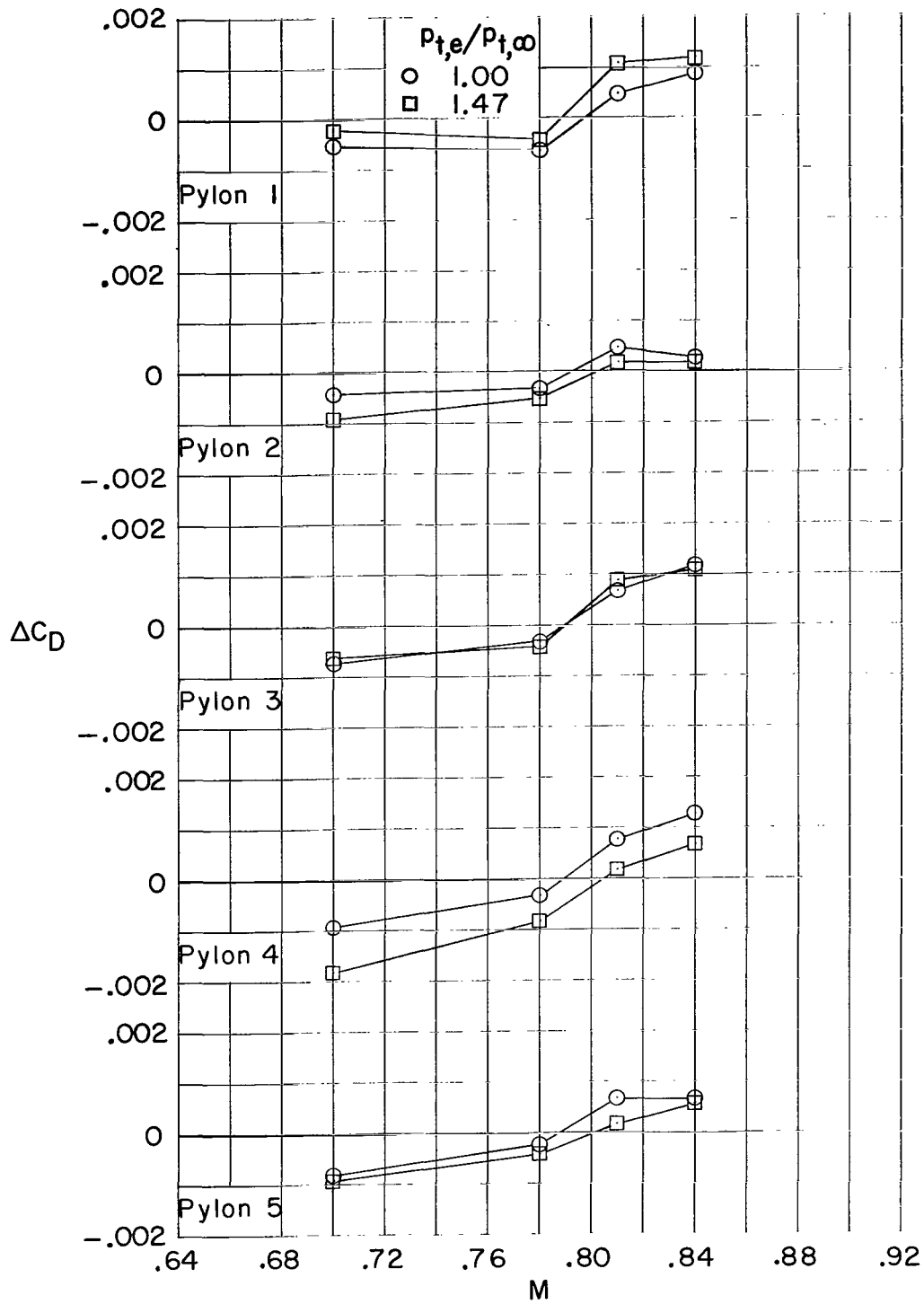
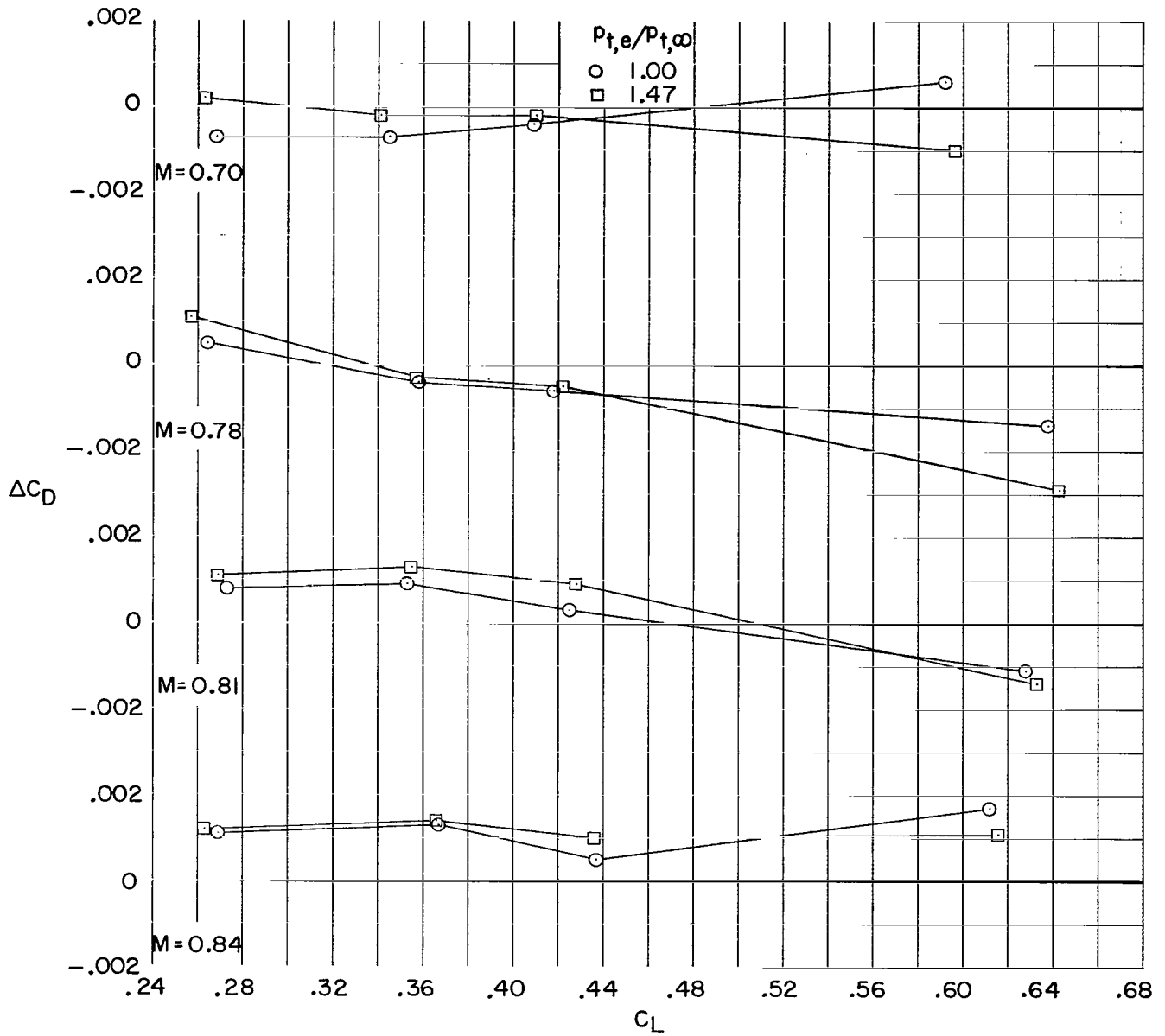
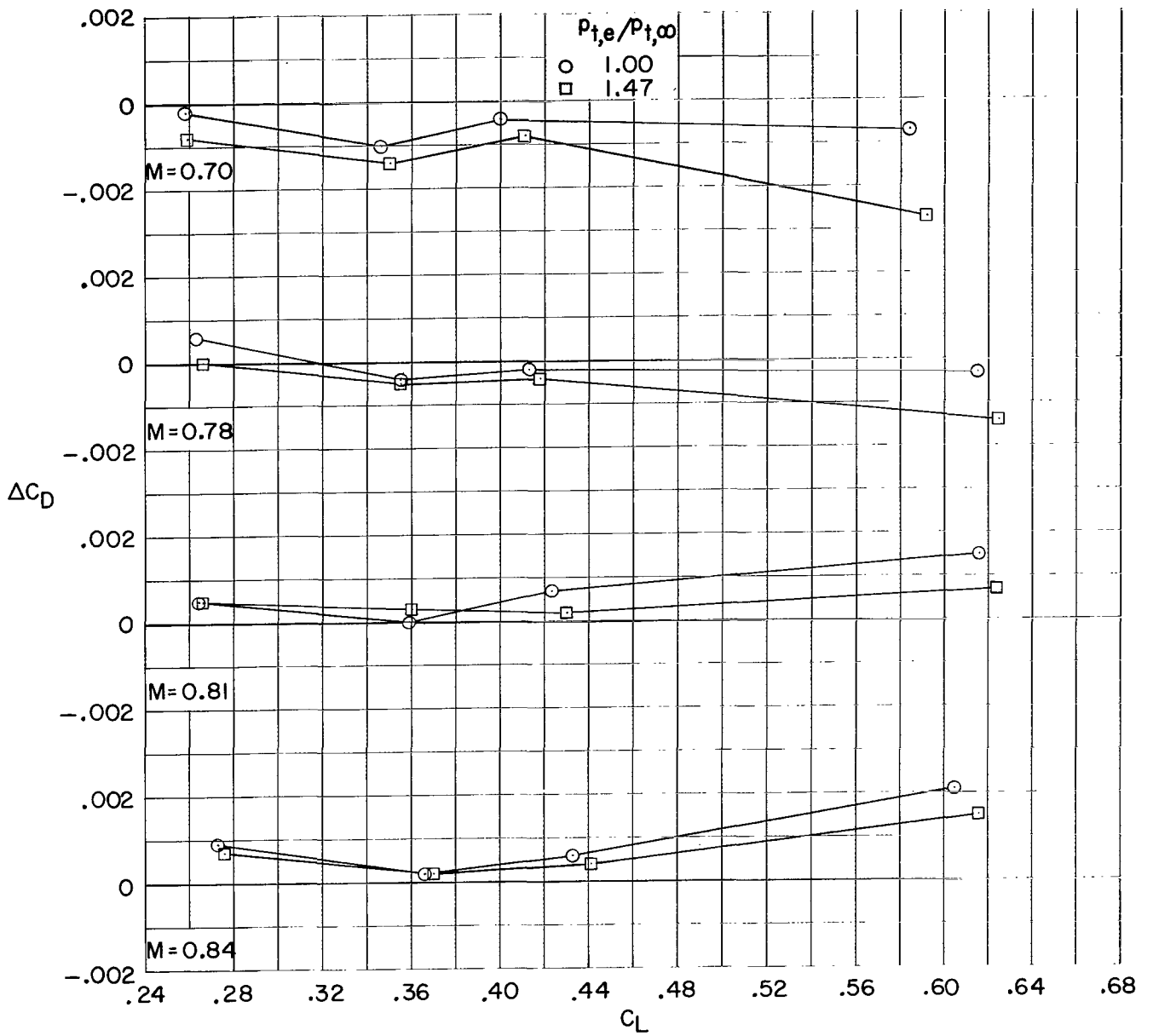


Figure 9.- Variation of the aerodynamic interference-drag coefficient with Mach number at a lift coefficient of 0.4 for the five engine positions.



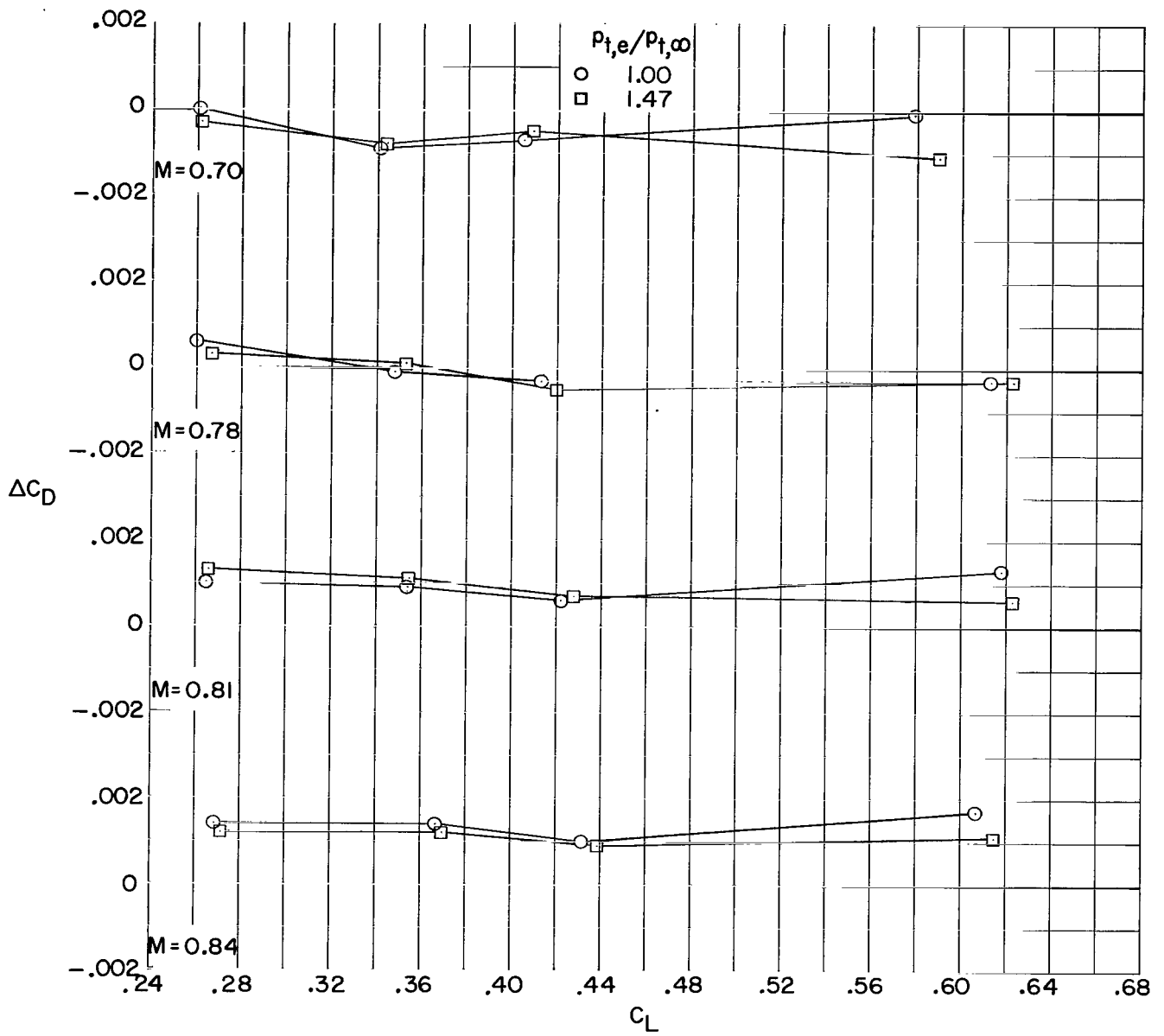
(a) Pylon 1.

Figure 10.- Variation of the aerodynamic interference-drag coefficient with lift coefficient at each test Mach number for the five engine positions.



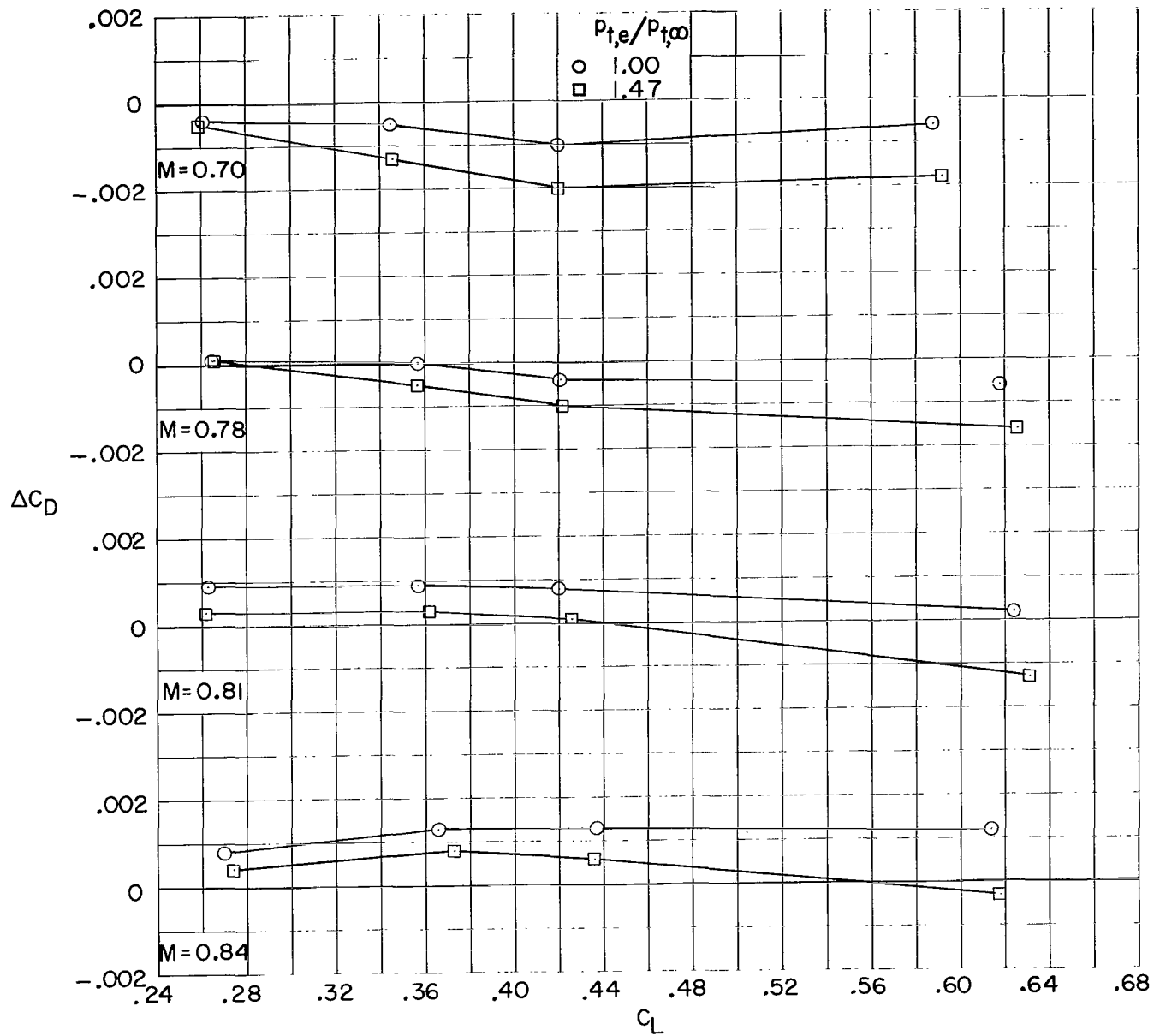
(b) Pylon 2.

Figure 10.- Continued.



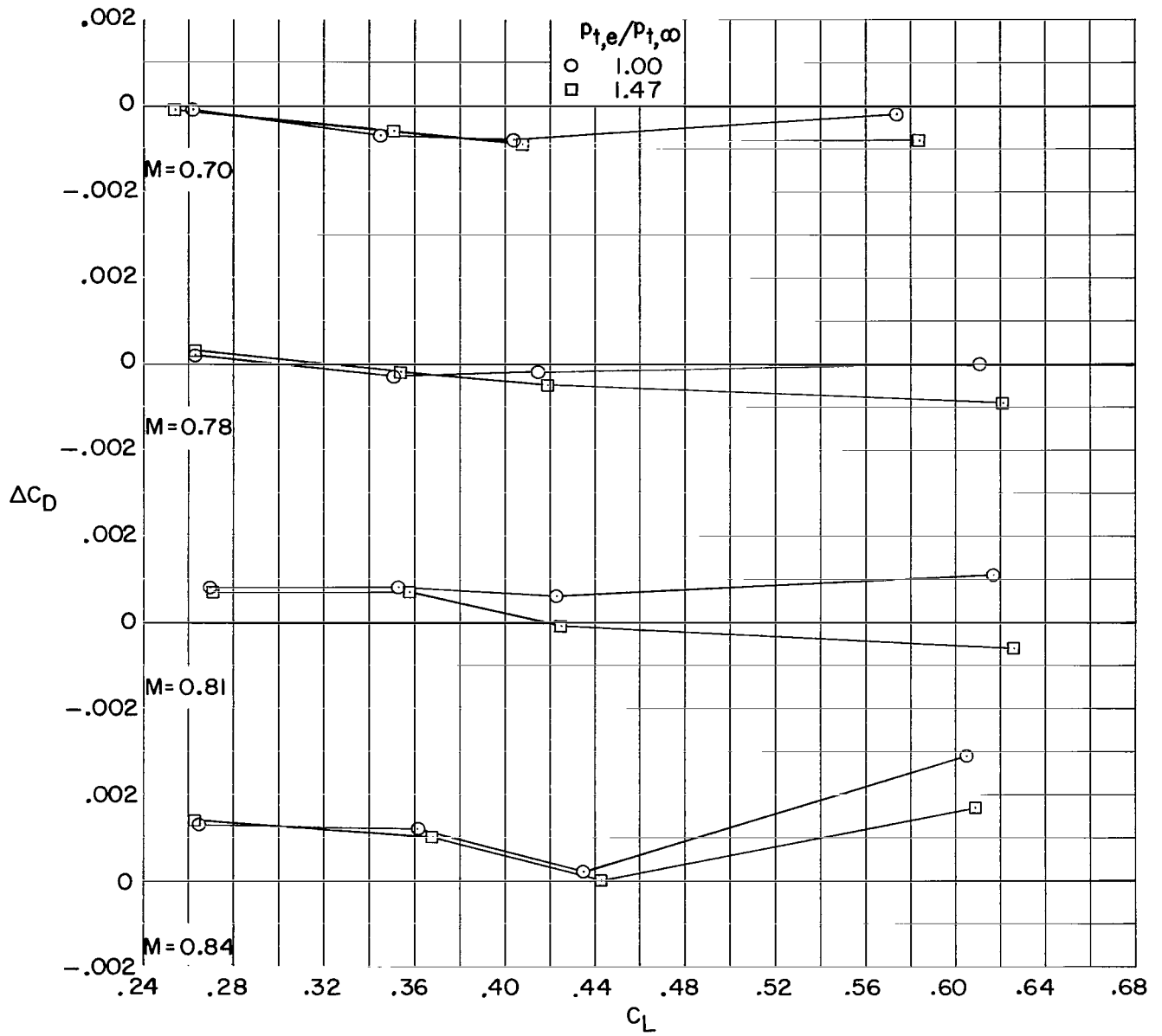
(c) Pylon 3.

Figure 10.- Continued.



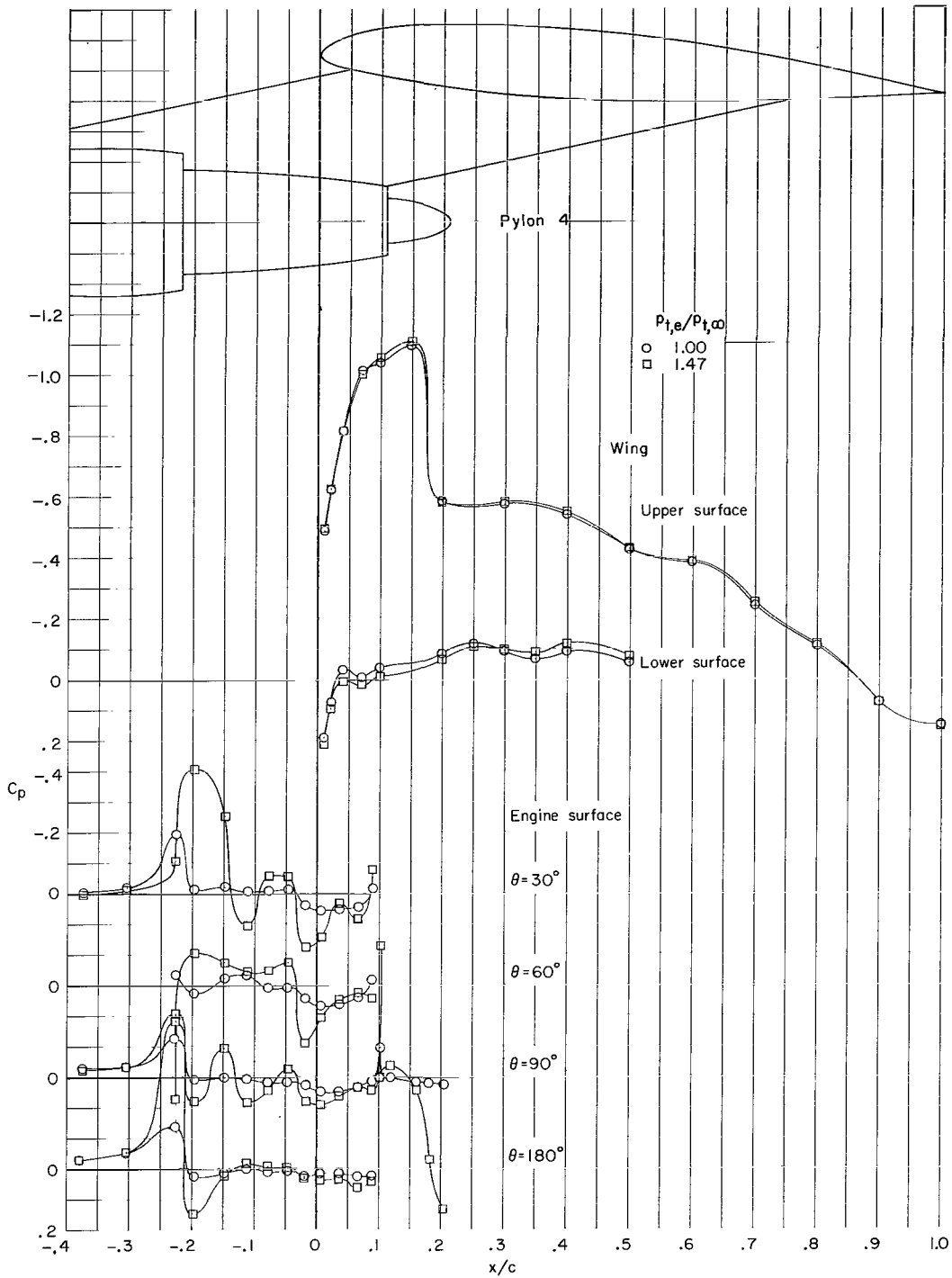
(d) Pylon 4.

Figure 10.- Continued.



(e) Pylon 5.

Figure 10.- Concluded.



(a) Outboard surfaces.

Figure 11.- Pressure distribution plots for wing and engine (fan cowl, turbine, and plug) surfaces for two fan-exit total-pressure ratios. Pylon 4 configuration; $M = 0.78$; $\alpha = 1.58^\circ$.



(b) Inboard surfaces.

Figure 11.- Concluded.

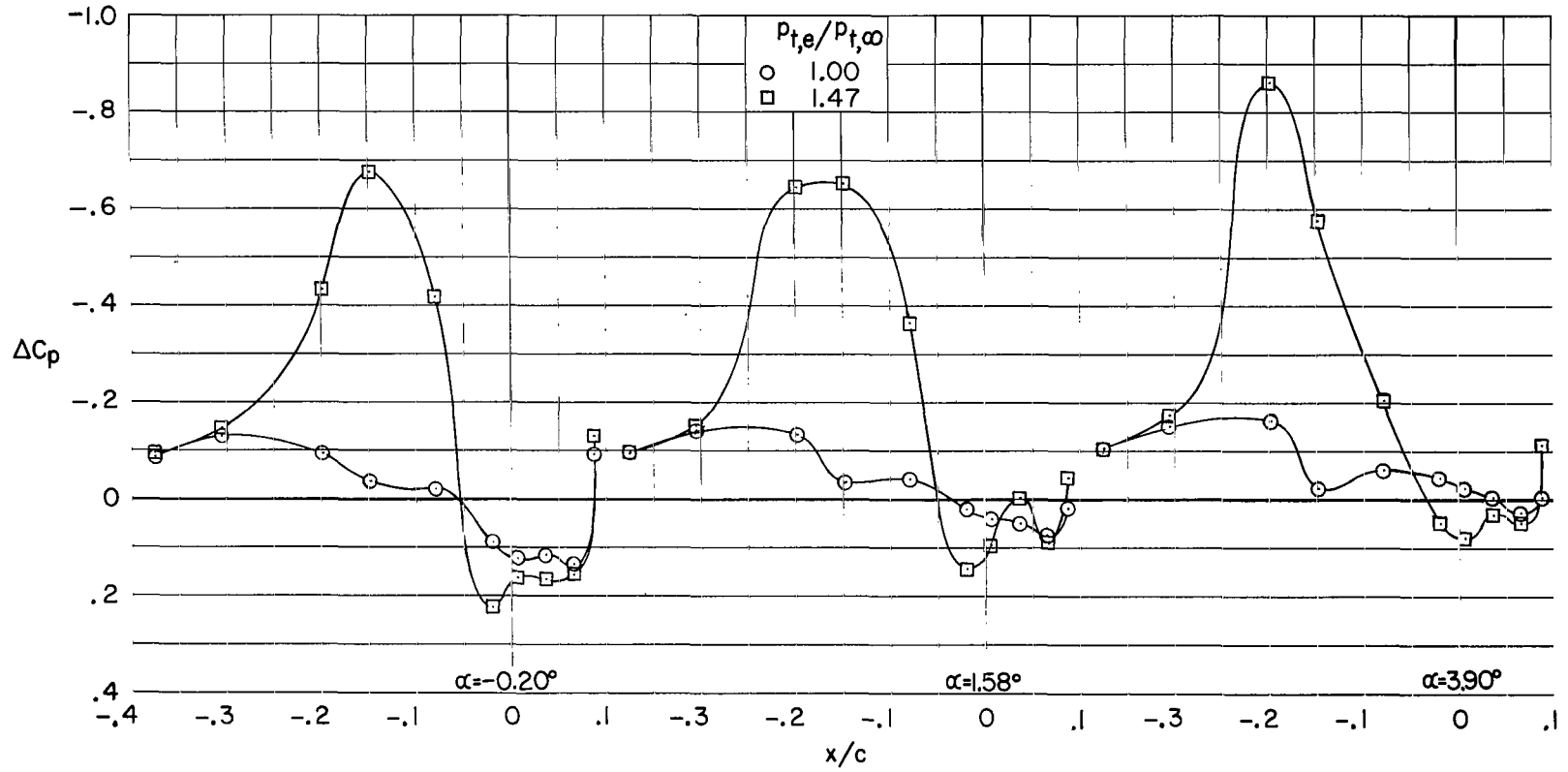


Figure 12.- Difference in pressure coefficients of the outboard surface of the engine and the inboard surface of the engine at the engine-pylon juncture ($\Delta C_p = C_{p,\theta=30^\circ} - C_{p,\theta=330^\circ}$) plotted against longitudinal distance from the wing leading edge. $M = 0.78$.

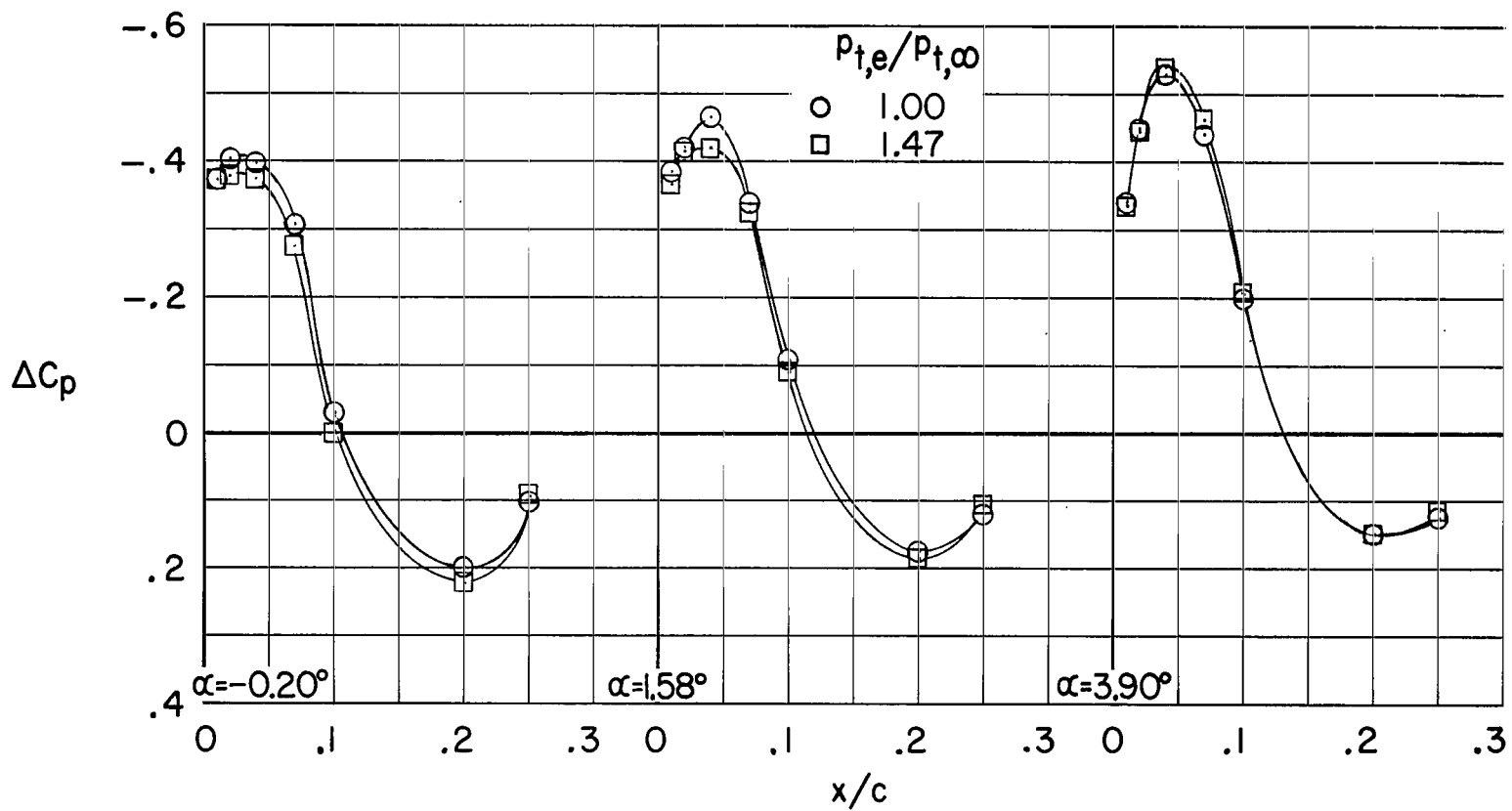


Figure 13.- Differential pressure coefficient of the wing lower surface ($\Delta C_p = (C_p)_{\text{outboard of pylon}} - (C_p)_{\text{inboard of pylon}}$) plotted against longitudinal distance from the wing leading edge. $M = 0.78$.

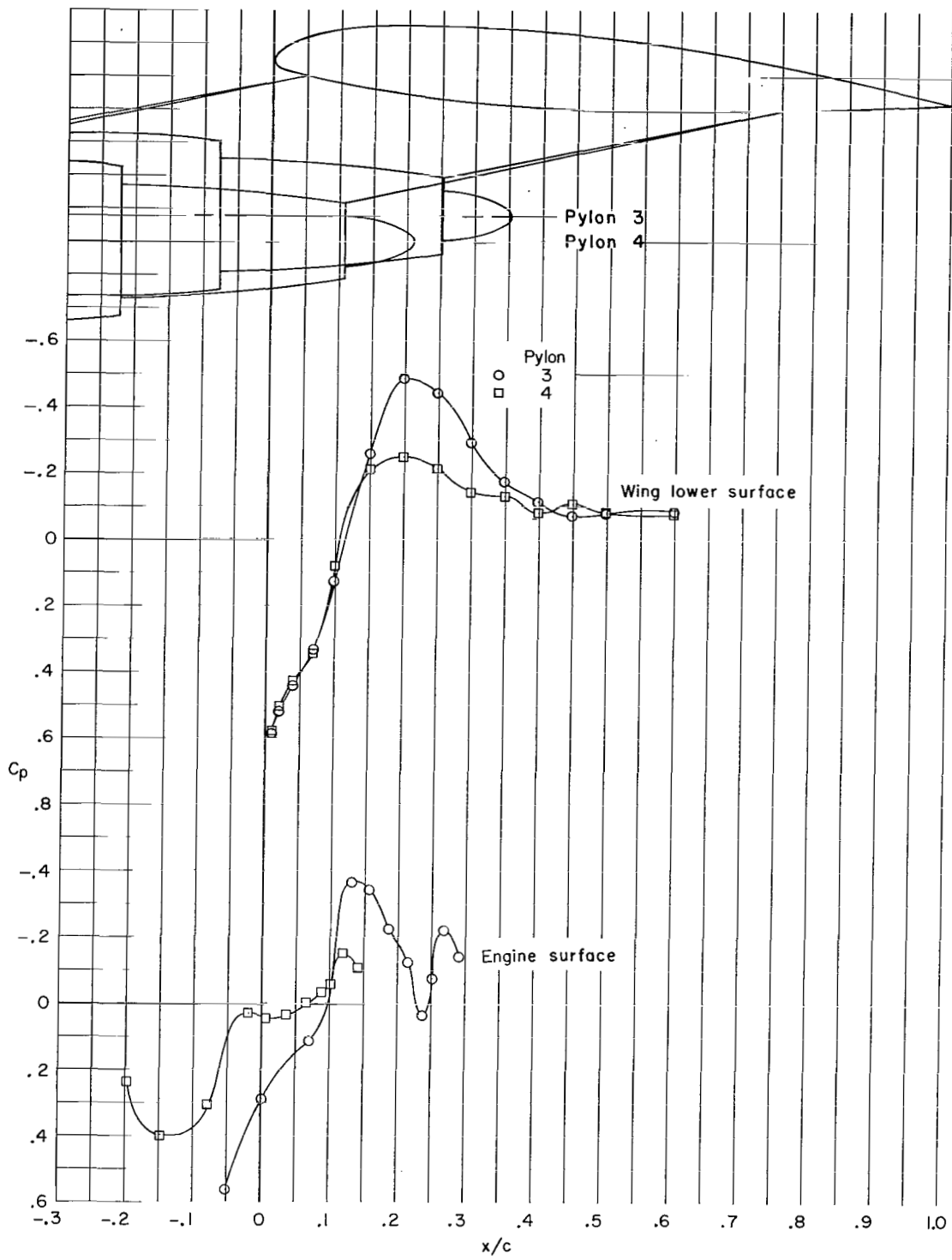


Figure 14.- Effect of engine position on the pressure coefficients for the wing lower surface inboard of the pylon (span station, 51.05 cm) and for the engine surface inboard of the pylon ($\theta = 330^\circ$). $M = 0.78$; $\alpha = 1.58^\circ$; $P_{t,e}/P_{t,\infty} = 1.47$.

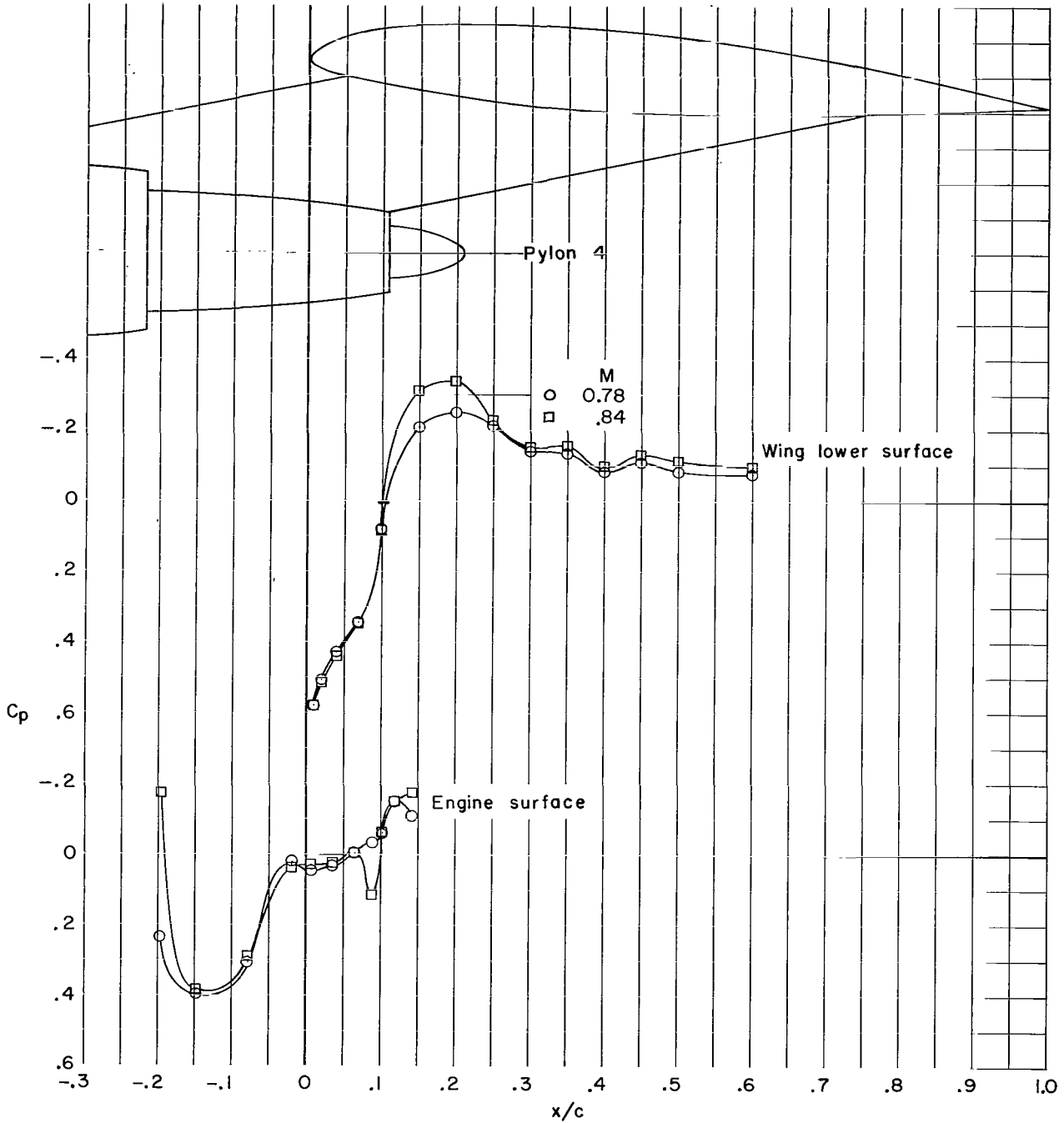


Figure 15.- Effect of Mach number on the pressure coefficients for the wing lower surface inboard of the pylon (span station, 51.05 cm) and for the engine surface inboard of the pylon ($\theta = 330^\circ$). Pylon 4; $\alpha = 1.58^\circ$; $p_{t,e}/p_{t,\infty} = 1.47$.

FIRST CLASS MAIL

06U 00L 26 51 3DS 68194 00903
AIR FORCE WEAPONS LABORATORY/AFWL/
KIRTLAND AIR FORCE BASE, NEW MEXICO 8711

ATT MISS MADELINE F. CANOVA, CHIEF TECHN
LIBRARY /WLIL/

POSTMASTER: If Undeliverable (Section 158
Postal Manual) Do Not Return

"The aeronautical and space activities of the United States shall be conducted so as to contribute . . . to the expansion of human knowledge of phenomena in the atmosphere and space. The Administration shall provide for the widest practicable and appropriate dissemination of information concerning its activities and the results thereof."

— NATIONAL AERONAUTICS AND SPACE ACT OF 1958

NASA SCIENTIFIC AND TECHNICAL PUBLICATIONS

TECHNICAL REPORTS: Scientific and technical information considered important, complete, and a lasting contribution to existing knowledge.

TECHNICAL NOTES: Information less broad in scope but nevertheless of importance as a contribution to existing knowledge.

TECHNICAL MEMORANDUMS: Information receiving limited distribution because of preliminary data, security classification, or other reasons.

CONTRACTOR REPORTS: Scientific and technical information generated under a NASA contract or grant and considered an important contribution to existing knowledge.

TECHNICAL TRANSLATIONS: Information published in a foreign language considered to merit NASA distribution in English.

SPECIAL PUBLICATIONS: Information derived from or of value to NASA activities. Publications include conference proceedings, monographs, data compilations, handbooks, sourcebooks, and special bibliographies.

TECHNOLOGY UTILIZATION PUBLICATIONS: Information on technology used by NASA that may be of particular interest in commercial and other non-aerospace applications. Publications include Tech Briefs, Technology Utilization Reports and Notes, and Technology Surveys.

Details on the availability of these publications may be obtained from:

SCIENTIFIC AND TECHNICAL INFORMATION DIVISION
NATIONAL AERONAUTICS AND SPACE ADMINISTRATION
Washington, D.C. 20546